

## NRC Publications Archive Archives des publications du CNRC

### **Multiphase modelling of water evaporation and condensation in an air-heated porous medium**

Zanoni, Marco A. B.; Wang, Jiahao; Torero, José L.; Gerhard, Jason I.

This publication could be one of several versions: author's original, accepted manuscript or the publisher's version. / La version de cette publication peut être l'une des suivantes : la version prépublication de l'auteur, la version acceptée du manuscrit ou la version de l'éditeur.

For the publisher's version, please access the DOI link below. / Pour consulter la version de l'éditeur, utilisez le lien DOI ci-dessous.

#### **Publisher's version / Version de l'éditeur:**

<https://doi.org/10.1016/j.applthermaleng.2022.118516>

*Applied Thermal Engineering*, 212, C, 2022-04-18

#### **NRC Publications Archive Record / Notice des Archives des publications du CNRC :**

<https://nrc-publications.canada.ca/eng/view/object/?id=5755cfca-8ef3-44d2-88d5-fb70b35686bf>

<https://publications-cnrc.canada.ca/fra/voir/objet/?id=5755cfca-8ef3-44d2-88d5-fb70b35686bf>

Access and use of this website and the material on it are subject to the Terms and Conditions set forth at

<https://nrc-publications.canada.ca/eng/copyright>

READ THESE TERMS AND CONDITIONS CAREFULLY BEFORE USING THIS WEBSITE.

L'accès à ce site Web et l'utilisation de son contenu sont assujettis aux conditions présentées dans le site

<https://publications-cnrc.canada.ca/fra/droits>

LISEZ CES CONDITIONS ATTENTIVEMENT AVANT D'UTILISER CE SITE WEB.

**Questions?** Contact the NRC Publications Archive team at

PublicationsArchive-ArchivesPublications@nrc-cnrc.gc.ca. If you wish to email the authors directly, please see the first page of the publication for their contact information.

**Vous avez des questions?** Nous pouvons vous aider. Pour communiquer directement avec un auteur, consultez la première page de la revue dans laquelle son article a été publié afin de trouver ses coordonnées. Si vous n'arrivez pas à les repérer, communiquez avec nous à PublicationsArchive-ArchivesPublications@nrc-cnrc.gc.ca.

# Multiphase Modelling of Water Evaporation and Condensation in an Air-Heated Porous Medium

Marco A. B. Zanoni <sup>a,c,\*</sup>, Jiahao Wang <sup>a</sup>, José L. Torero <sup>b</sup>, Jason I. Gerhard <sup>a</sup>

<sup>a</sup> Department of Civil and Environmental Engineering, University of Western Ontario, London, Ontario, N6A 5B9, Canada

<sup>b</sup> Department of Civil, Environmental and Geomatic Engineering, University College London, UK

<sup>c</sup> Construction Research Centre, National Research Council Canada, Ottawa, Ontario, Canada

\* Corresponding author at: Department of Civil and Environmental Engineering, The University of Western Ontario, Claudette Mackay-Lassonde Pavilion, Rm. 1317, London, Ontario, Canada N6A 5B9. E-mail address: mbazelat@uwo.ca (M.A.B. Zanoni).

## Abstract

Moisture transport as well as evaporation and condensation are key mechanisms in the energy management of many processes occurring in different porous media. The role of moisture varies significantly among several applications such as food drying, concrete heating, deep geological barriers, and smouldering combustion of wet fuels. Currently, there is a lack of numerical models able to accurately predict these processes within a complex porous matrix. A one-dimensional numerical model was developed to predict the transient and spatial movement of evaporative and condensation fronts in an air heated inert porous bed partially saturated with water. The results showed that by introducing simple calibration constants in the effective thermal properties, the model was able to accurately predict experimental results. The numerical results revealed that temperatures rapidly increase to boiling conditions because of vapour condensation. Moreover, the model identified that the temperature plateau occurred because all the available energy was used to evaporate water. Evaporative cooling was also predicted and showed a rapid temperature decrease when air was initiated. When the air supply was initiated along with the heater, evaporative cooling resulted in a temperature plateau lower than air-off conditions. This was caused because vapour was carried forward much faster by the forced air, resulting in lower condensation and consequently lower energy released. Overall, this work provides a valuable representation in space and time of the key moisture transport processes in the gas phase as well as key phase-change and heat transfer processes occurring in porous media.

**Keywords:** Evaporation, Condensation, Boiling, Phase-Change, Porous Media, Evaporative Cooling

## Nomenclature

### *Latin Letters*

$A_s$	Surface area, m <sup>2</sup>
$C_p$	Specific heat capacity, J kg <sup>-1</sup> K <sup>-1</sup>
$d_p$	Particle diameter, mm
$D$	Diffusion coefficient, m <sup>2</sup> s <sup>-1</sup>
$E$	Energy, J
$\dot{E}$	Energy rate, J s <sup>-1</sup>
$h_{sg}$	Interfacial heat transfer coefficient, W m <sup>-2</sup> K <sup>-1</sup>
$h_g$	Hubbert's potential, m
$k$	Thermal conductivity, W m <sup>-1</sup> K <sup>-1</sup>
$k_{evap}$	Equilibrium time constant, s <sup>-1</sup>
$k_p$	Intrinsic permeability, m <sup>2</sup>
$m$	Mass, kg
$\dot{m}$	Mass flow, kg s <sup>-1</sup>
$\dot{m}_w'''$	Evaporation rate, kg m <sup>-3</sup> s <sup>-1</sup>
$M$	Molar weight, g mol <sup>-1</sup>
$Nu$	Nusselt number
$P$	Pressure, Pa
$Pr$	Prandtl number
$\dot{q}''$	Heat flux, W m <sup>-2</sup>
$r$	Column radius, m
$R$	Ideal gas constant, J K <sup>-1</sup> mol <sup>-1</sup>
$Re$	Reynolds number
$S$	Saturation
$T$	Temperature, K
$u_g$	Darcy air flux, m s <sup>-1</sup>
$U$	Global heat loss coefficient, W m <sup>-2</sup> K <sup>-1</sup>
$V$	Volume, m <sup>3</sup>
$Y$	Mass fraction

$w$  Humidity

*Greek Symbols*

$\Delta H_{evap}$  Heat of evaporation, MJ kg<sup>-1</sup>

$\rho$  Density, kg m<sup>-3</sup>

$\phi$  Porosity

$\sigma$  Stefan–Boltzmann constant, W m<sup>-2</sup> K<sup>-4</sup>

$\mu$  Dynamic viscosity, Pa.s

*Subscripts/Superscript*

$a$  Air

$Cl$  Cylinder

$eff$  Effective

$evap$  Evaporation

$f$  Final

$g$  Gas

$in$  Inlet

$0$  Ambient

$rad$  Radiation

$s$  Solid/sand

$rel$  Relative

$sat$  Saturation

$sp$  Sphere

$spec$  Specific

$v$  Vapour

$w$  Water

## 1. Introduction

Moisture transport as well as evaporation and condensation are key mechanisms in the energy management of many processes occurring in porous media. Water evaporation and condensation have been studied in different porous media such as packed bed [1, 2], bare soils [3], deep geological repositories for radioactive waste [4], oil reservoirs [5, 6], food [7-13], concrete [14], wood [15], peat [16], and organic fuels embedded in sand [17, 18]. The role of moisture varies significantly among these applications and therefore the approaches and assumptions used to model evaporation and condensation are also different. Food drying, concrete spalling and contaminated soil remediation are three well documented examples that illustrate the variety of applications.

In food drying, the removal of moisture reduces microbiological activity (e.g., mold growth), improving food storage and conservation [10]. Convective drying is typically used, where forced air with low relative humidity is applied at the food surface [8, 9]. Moisture moves through capillary forces and diffusion due to a difference in concentration from the interior (wet) to the surface (dry) [7, 11, 15, 19]. In this case, the controlling mechanisms relate primarily to the migration of water towards the surface. Numerical models that simulate this application typically introduce complexity in the characterization of the porous media (e.g., shrinkage [20, 21]), but evaporation and condensation are generally neglected.

Understanding water evaporation is also important for building materials under fire conditions. When concrete is exposed to a high heat flux, bound water initially trapped in the material quickly evaporates. The escaping water vapour passes through regions of low permeability, which can increase the pore pressure and result in the formation of cracks or even concrete spalling [14]. Related studies have focused on detailed modelling of evaporation, permeability, and the resulting pore pressures [22] while condensation and vapour transport tend to be simplified.

Designing thermal remediation systems for contaminated soil requires the quantitative consideration of water evaporation as it represents a major heat sink. Methods using bulk heating of contaminated soil can treat this problem by means of simple heat-sink approximations, while dynamic systems such as smouldering of contaminated soils require a more comprehensive mathematical framework. Smouldering has been successfully applied to destroy wastes considered challenging due to their high moisture content (e.g., feces [17] and biosolids [18]). At low and moderate moisture contents ( $< 70\%$ ), the pre-heated air evaporates the water, which condenses in the cold regions ahead of the smouldering reaction. Hence, the propagation of the smouldering front occurs in the dried material, i.e., there is a separation of the

smouldering and evaporation fronts [5, 17]. At high moisture contents ( $> 70\%$ ), the smouldering reaction may not overcome the energy sink caused by water evaporation and both smouldering and evaporation fronts collapse into one, resulting in extinction of the combustion reaction [17, 18]. Note that in these studies liquid phase water migration can be ignored, nevertheless, if the characteristic length (i.e., large) and time scales (i.e., long) allow for buoyancy to become relevant, then water mobility needs to be considered [23-26]. Similar processes occur during natural smouldering of peatlands. However, in this case, a high moisture content is required to prevent homogeneous combustion (i.e., flame) and the ensuing fire spread [16]. In both cases, evaporation and condensation require models that characterize moisture content in time and space.

Given the complexities associated to most of these applications, even the most simplified representations require the use of numerical models. One of the most-often applied models to describe and quantify water evaporation is the diffusion model, which assumes that i) liquid moves by diffusion from the interior to the solid surface, where it evaporates and moves into the air, and ii) liquid evaporates at the solid interior and the water vapour diffuses to the solid surface and then moves into the air [27]. The conceptual formulation of these models allows them to be adapted to a large variety of applications. Philip and De Vries [28] extended the diffusion model by including heat and mass transfer, capillary flow, and the interactions between vapor, liquid, and solid phases. This extended evaporation model was widely applied due to its simple applicability.

In the late 1970s, Whitaker [19] and Whitaker and Chou [29], improved the gas phase transport processes by introducing volume-averaged transport equations which include the liquid and vapour phase continuity equations, moisture transport through Darcy's law and capillary action. The main simplification is that liquid, solid and vapour phase energy equations are combined into a single temperature equation. This limited formulation provides the existing framework for numerical modeling of water evaporation in porous media.

Numerical models simulate water evaporation and condensation based on Local Thermal Equilibrium (LTE) [7, 11, 12, 15, 30, 31] and Local Thermal Non-Equilibrium [8, 9, 32-36] conditions. LTE is generally used because is numerically simple, i.e., it assumes equal temperature for the gas (dry air and vapour), solid (matrix) and liquid (water, oil) phases. A similar approach is used for mass transfer, where two assumptions are identified: equilibrium [5, 12, 15, 30, 31] and non-equilibrium [7-9, 11, 37]. Equilibrium mass transfer assumes that the water vapour concentration in the air is always equal to its equilibrium (or saturation) value, which means phase-change is instantaneous, i.e., the time associated

with evaporation and condensation is negligible [12, 38]. In non-equilibrium mass transfer, the phase-change between liquid water and vapour, is driven by a difference in concentration between the vapour and saturated phases, and the magnitude of this difference is an indicator of how far a system is away from equilibrium.

Several formulations describing the non-equilibrium approach have been tested in the literature [3], based on irreversible thermodynamics, first-order reaction kinetics, or the kinetic theory of gases. Each formulation has a phenomenological coefficient (equilibrium time coefficient,  $k_{evap}$ ) that is either physically- or empirically-based and is often used as a fitting parameter. Non-equilibrium mass transfer typically provides better results than equilibrium [3].

The complex interactions of the multiple processes make it challenging to establish the controlling mechanisms. Thus, it is beneficial to explore individual aspects numerically with simpler one-dimensional models coupled with experimental data. Currently, there is a lack of such models, although evaporation and condensation within a complex porous matrix are common in numerous engineering systems [17, 18]. This study develops and validates a multiphase model for dynamic water evaporation and condensation fronts in porous media including heat transfer and phase-change processes evolving in space and time. The fronts are subject to one-dimensional, heated air injection, following engineering applications. Experiments with and without heat were used to validate the model. The effects of water evaporation and condensation on the global energy balance were analyzed and a global mass balance was developed. Furthermore, the influence of the air flow rate and heating source, along with three main process parameters, were examined via a model sensitivity analysis. This work provides unique insight into evaporative cooling and water evaporation and condensation in a heated porous bed. Moreover, it is expected to provide the basis for simulating such processes in complex systems, such as smouldering combustion of wet fuels and thermo-hydro-mechanical processes in deep geological repositories for radioactive waste.

## **2. Methodology**

### *2.1. Modelling*

This work further develops the modelling approach provided in [39]. The multiphase model followed the theory of drying developed by Whitaker [19] and takes into account three phases: solid (sand grains), liquid (water), and gas (air and water vapour). The solid phase is stationary, i.e.,  $u_s = 0$ . The conservation of mass for liquid water:

$$\phi \rho_w \frac{\partial(S_w)}{\partial t} = \dot{m}_w''' \quad (1)$$

assumes that liquid water is also immobile ( $u_w = 0$ ) [5, 37], constant water density ( $\rho_w$ ), and negligible capillary effects. The total porosity ( $\phi$ ) is defined as the volume fraction occupied by gas ( $\phi_g = \phi S_g$ ) and water ( $\phi_w = \phi S_w$ ), i.e.,  $\phi = \phi_w + \phi_g$ , where the water saturation ( $S_w$ ) is the fraction of pore volume occupied by water and the gas saturation ( $S_g$ ) is the fraction of pore volume occupied by gas ( $S_g = 1 - S_w$ ). The dependent variable in Eq. (1) is  $S_w$ . Equation (1) also assumes that liquid water is becoming water vapour (negative evaporation rate,  $\dot{m}_w'''$ , see Eq. (14)).

The mass fraction of water vapour ( $Y_v$ ) was calculated via the air-water vapour transport equation [40]:

$$\frac{\partial(\phi S_g \rho_g Y_v)}{\partial t} + \frac{\partial(\rho_g u_g Y_v)}{\partial x} = \frac{\partial}{\partial x} \left( \phi S_g \rho_g D_{eff} \frac{\partial Y_v}{\partial x} \right) + \dot{m}_w''' \quad (2)$$

The effective diffusivity ( $D_{eff}$ ) is a forward gas phase diffusion coefficient and does not represent mass transfer between the liquid and the gas phases. Note that the flow contributions in the dispersion terms were assumed to be negligible. In the literature [41, 42],  $D_{eff}$  is typically calculated by:

$$D_{eff} = D_g (S_g \phi)^{4/3} \quad (3)$$

where  $D_g$  is the diffusion coefficient. However, in this work,  $D_{eff}$  was calibrated (see Section 3.2.1). Equation (2) also assumes that air and water vapour are moving with the same Darcy velocity ( $u_g$ ) [7, 8, 11, 30, 43]:

$$u_g = - \frac{k_p}{\mu_g} \frac{\partial P_g}{\partial x} \quad (4)$$

without gravity effects, where  $k_p$  is the intrinsic permeability,  $\mu_g$  is the gas dynamic viscosity, and  $P_g$  is the total gas pressure.  $\mu_g$  is calculated based on  $Y_v$  [11]:

$$\mu_g = \mu_a (1 - Y_v) + \mu_v (Y_v) \quad (5)$$

where  $\mu_a$  and  $\mu_v$  are the dynamic viscosities of air and water vapour.

The gas pressure ( $P_g$ ) was calculated via the air-water vapour continuity equation:

$$\frac{\partial(\phi S_g \rho_g)}{\partial t} + \frac{\partial(\rho_g u_g)}{\partial x} = \dot{m}_w''' \quad (6)$$

where the total gas density ( $\rho_g$ ) followed the ideal gas law and Dalton's law [44]:



$$\rho_g = \rho_a + \rho_v = \frac{P_g}{R_g T_g} \quad (7)$$

and:

$$\rho_a = \frac{P_a}{R_a T_g} \quad (8)$$

$$\rho_v = \frac{P_v}{R_v T_g} \quad (9)$$

$$P_a = P_g - P_v \quad (10)$$

$$R_g = R_a(1 - Y_v) + R_v(Y_v) \quad (11)$$

where  $\rho_a$  and  $\rho_v$  are the air and water vapour densities,  $P_a$  and  $P_v$  are the partial pressure of air and water vapour,  $R_a$  and  $R_v$  are the specific gas constants of air and water vapour.  $P_v$  was calculated as a function of  $Y_v$  and  $P_g$  [8]:

$$P_v = \frac{Y_v R_v P_g}{R_a + Y_v(R_v - R_a)} \quad (12)$$

$$R_i = \frac{R}{M_i} \text{ with } i = a, v \quad (13)$$

where  $R$  is the ideal gas constant,  $M$  is the molar weight, and  $i$  is the gas species (i.e., air and water vapour). Further detail on the derivation of Eq. (12) is given in [8].

The evaporation rate ( $\dot{m}_w'''$ ) uses unrestricted non-equilibrium mass transfer [3, 7, 8, 11, 45] as the limiting mass transfer process:

$$\dot{m}_w''' = k_{evap} \left( \frac{1}{R_v T_g} \right) (P_v - P_{sat}) \quad (14)$$

$k_{evap}$  is the evaporation constant and is defined as the inverse of the time,  $\Delta t^{-1}$  ( $s^{-1}$ ), necessary to reach equilibrium mass transfer in the system [3, 7, 11, 46]. For large  $k_{evap}$  values (e.g.,  $> 5 \text{ s}^{-1}$ ), equilibrium mass transfer is reached, and phase-change occurs instantaneously. This was observed by negligible temperature changes when  $k_{evap} > 5 \text{ s}^{-1}$ . Therefore, the non-equilibrium mass transfer formulation presented in Eq. (14) is valid for  $k_{evap} < 5 \text{ s}^{-1}$  ( $k_{evap} \geq 5 \text{ s}^{-1}$  results in equilibrium mass transfer) and  $0.100 \leq x \leq 0.465 \text{ m}$ , i.e., in the regions initially wet ( $0.100 \leq x \leq 0.300 \text{ m}$ ) and initially dry ( $0.300 < x \leq 0.465 \text{ m}$ ) where condensation occurred.

The saturation pressure ( $P_{sat}$ ) was represented by the Buck equation [47, 48]:

$$P_{sat} = 610.78 \exp\left(\frac{17.27T_g}{T_g + 237.3}\right) \quad (15)$$

where  $P_{sat}$  is in Pa and the gas temperature ( $T_g$ ) is in degree Celsius. In Eq. (14), condensation occurs when  $P_v > P_{sat}$ , whereas evaporation takes place when  $P_v < P_{sat}$ . Boiling occurs when  $P_v = P_{sat}$ ; therefore, Eq. (14) cannot predict boiling.

The model solved the transient energy equation for both solid ( $T_s$ ) and gas ( $T_g$ ) phases [8, 19, 45, 49]:

$$(\rho C_p)_{eff} \frac{\partial T_s}{\partial t} = \frac{\partial}{\partial x} \left( k_{eff} \frac{\partial T_s}{\partial x} \right) + h_{sg} \left( \frac{A_{s,sp}}{V_{sp}} \right) (T_g - T_s) - U \left( \frac{A_{s,cl}}{V_{cl}} \right) (T_s - T_0) + \Delta H_{evap} \dot{m}_w''' \quad (16)$$

$$\begin{aligned} \phi S_g \rho_g C_{pg} \frac{\partial T_g}{\partial t} + \rho_g C_{pg} u_g \frac{\partial T_g}{\partial x} \\ = \frac{\partial}{\partial x} \left( \phi S_g k_g \frac{\partial T_g}{\partial x} \right) + h_{sg} \left( \frac{A_{s,sp}}{V_{sp}} \right) (T_s - T_g) + \dot{m}_w''' C_{pv} (T_s - T_g) \end{aligned} \quad (17)$$

where the effective “*eff*” properties followed a linear average [45]:

$$(\rho C_p)_{eff} = (1 - \phi) \rho_s C_{ps} + (\phi S_w) \rho_w C_{pw} \quad (18)$$

$$(k)_{eff} = (1 - \phi)(k_s + k_{rad}) + (\phi S_w) k_w \quad (19)$$

$$C_{pg} = (1 - Y_v) C_{pa} + Y_v C_{pv} \quad (20)$$

$$k_g = (1 - Y_v) k_a + Y_v k_v \quad (21)$$

where  $\rho_s$  and  $\rho_w$  are the particle density and water density, and  $C_{ps}$ ,  $C_{pw}$ ,  $C_{pa}$ , and  $C_{pv}$  are the sand, water, air, and water vapour heat capacities, respectively.  $k_s$ ,  $k_w$ ,  $k_a$ , and  $k_v$  are the sand, water, air, and water vapour thermal conductivities. Radiation heat transfer (“*rad*”) followed the Rosseland approximation and was expressed as a radiative conductivity ( $k_{rad} = 16\sigma d_p T_s^3/3$ ) [39], where  $\sigma$  is the Stefan–Boltzmann constant.

Equation (16) assumes that the porous medium was homogeneous and sand particles were taken as spheres ( $A_{s,sp}/V_{sp} = 6(1-\phi)/d_p$ ). Liquid water and sand are assumed to be in local thermal equilibrium forming the “solid” phase. This is a reasonable assumption since water behaves as a film coating the sand. Therefore, the contact surface area is assumed to be sufficiently large, compared to the thickness of the water film, for internal temperature relaxation to occur before any gas phase temperature changes. Moreover, Eq. (16) also shows that the volumetric energy for evaporation ( $\Delta H_{evap} \dot{m}_w'''$ ) is completely transferred from the solid to the gas phase, which is accounted for in Eq. (17) by the addition of a phase temperature-dependent term ( $\dot{m}_w''' C_{pv} (T_s - T_g)$ ) [49].

Local Thermal Non-Equilibrium (LTNE) between solid and gas phases was considered by applying the interfacial heat transfer coefficient ( $h_{sg}$ ) according to the empirical Nusselt ( $Nu$ ) versus Reynolds ( $Re$ ) and Prandtl ( $Pr$ ) correlation developed specifically for heat transfer in porous media scenarios [39]:

$$Nu = \frac{h_{sg} d_p}{k_g} = 0.001(Re^{1.97} Pr^{1/3}) \quad (22)$$

Equation (22) has been shown to be adequate in simulations of applied smouldering processes [39, 50], which require forced air (i.e.,  $Re > 0$ ) to create the self-sustaining process. Evaporation for example, takes place even when the air flux is off (i.e.,  $\dot{m}_w''' < 0$  when  $0 \leq t \leq t_g$ ). In this case ( $Re = 0$ ), temperatures are relatively low, and energy transfer between solid and gas phases was assumed to occur instantaneously, i.e., Local Thermal Equilibrium (LTE) exists. This was represented by a very large  $h_{sg}$  ( $500 \text{ W m}^{-2} \text{ K}^{-1}$  [39]). When  $t > t_g$ , forced air is supplied ( $Re > 0$ ), temperature difference between phases increases, LTNE is created, and then  $h_{sg}$  follows Eq. (22).

The heat of evaporation in Eq. (16) was defined as in [51]:

$$\Delta H_{evap} = 2501.05 \times 10^3 \left( \frac{647.3 - T_s}{643.3 - 273.15} \right)^{0.3298} \quad (23)$$

with the solid temperature ( $T_s$ ) in Kelvin.

A global heat loss coefficient ( $U$ ) [39, 52] was included in Eq. (16) and used the surface area per unit volume ( $A_{s,cl}/V_{cl}=2/r$ ), where  $r$  is the radius of the column. The thermal properties of air, water, sand, and water vapour varied with temperature and are presented in Table 1 along with the model parameters. The initial and boundary conditions are defined in Table 2.

Table 1. Model Input Parameters for Base Case

Par.	Value	Unit	Ref.
$C_{ps}$	$2.49(T_s)+39.06$	$\text{J kg}^{-1} \text{K}^{-1}$	[39]
$C_{pa}$	$-3 \times 10^{-5}(T_g^2)+0.2261(T_g)+940.35$	$\text{J kg}^{-1} \text{K}^{-1}$	[53]
$C_{pv}$	$7 \times 10^{-5}(T_g^2)+0.5583(T_g)+1835.8$	$\text{J kg}^{-1} \text{K}^{-1}$	[53]
$C_{pw}$	$5.47 \times 10^{-6}(T_s^2)+9.086 \times 10^{-5}(T_s)+4.176$	$\text{J kg}^{-1} \text{K}^{-1}$	[21]
$d_p$	1.59	mm	This work
$D_{eff}$	$8 \times 10^{-5}$	$\text{m}^2 \text{s}^{-1}$	Calibrated
$k_s$	$0.000541(T_s)+0.1044$	$\text{W m}^{-1} \text{K}^{-1}$	[39]
$k_a$	$-1 \times 10^{-8}(T_g^2)+8 \times 10^{-5}(T_g)+4.3 \times 10^{-3}$	$\text{W m}^{-1} \text{K}^{-1}$	[53]
$k_v$	$4 \times 10^{-8}(T_g^2)+8 \times 10^{-5}(T_g)+0.0152$	$\text{W m}^{-1} \text{K}^{-1}$	[53]
$k_w$	$6.7 \times 10^{-5}(T_s^2)+1.76 \times 10^{-3}(T_s)+0.571$	$\text{W m}^{-1} \text{K}^{-1}$	[21]
$k_p$	$1.0 \times 10^{-9}$	$\text{m}^2$	[39]
$k_{evap}$	2.0	$\text{s}^{-1}$	Calibrated
$M_g$	28.97	$\text{g kg}^{-1}$	[44]
$M_v$	18.01	$\text{g kg}^{-1}$	[44]
$\phi$	0.37	-	[39]
$\rho_s$	2650	$\text{kg m}^{-3}$	[39]
$\rho_w$	995.74	$\text{kg m}^{-3}$	[21]
$P_{a,0}$	1.0133	kPa	[44]
$\dot{q}_{in}''$	25	$\text{kW m}^{-2}$	[39]
$r$	0.08	m	This work
$R$	8.314	$\text{J K}^{-1} \text{mol}^{-1}$	[44]
$R_a$	286.7	$\text{J kg}^{-1} \text{K}^{-1}$	[44]
$R_v$	461.5	$\text{J kg}^{-1} \text{K}^{-1}$	[44]
$S_{w,0}$	0.3	-	This work
$t_g$	4449	s	This work
$t_h$	4935	s	This work
$T_0$	293	K	This work
$u_{g,in}$	0.05	$\text{m s}^{-1}$	This work
$U$	1.7	$\text{W m}^{-2} \text{K}^{-1}$	[39]
$\gamma$	0.7	-	Calibrated
$\delta$	2.0	-	Calibrated
$\mu_a$	$-9 \times 10^{-12}(T_g^2)+4 \times 10^{-8}(T_g)+6 \times 10^{-6}$	Pa s	[53]
$\mu_v$	$7 \times 10^{-12}(T_g^2)+4 \times 10^{-8}(T_g)+9 \times 10^{-6}$	Pa s	[53]
$Y_{v,0}$	$1.43 \times 10^{-3}$	-	This work
$w_{spec,0}$	$1.43 \times 10^{-3}$	-	This work
$w_{rel,0}$	0.10	-	This work

Table 2. Initial and Boundary Conditions for Numerical Model.

Eq.	Initial Condition	Boundary Condition
(1)	$t = 0 \Rightarrow S_w = S_{w,0}$	-
(2)	$t = 0 \Rightarrow Y_v = Y_{v,0}^a$	$x = 0.000 \text{ m} \Rightarrow Y_v = Y_{v,0}^a$ $x = 0.465 \text{ m} \Rightarrow -\phi S_g \rho_g D_{eff} \frac{\partial(Y_v)}{\partial x} = \rho_g u_g (Y_{v,0} - Y_v)$
(6)	$t = 0 \Rightarrow P_g = P_{a,0} + P_{v,0} = P_{g,0}$	$x = 0.000 \text{ m} \Rightarrow \rho_{g,0} u_g(t) \rightarrow \begin{cases} u_g(t) = 0 \rightarrow 0 \leq t \leq t_g \\ u_g(t) = u_{g,in} \rightarrow t_g < t \leq t_f \end{cases}$ $x = 0.465 \text{ m} \Rightarrow P_g = P_{g,0}$
(16-17)	$t = 0 \Rightarrow T_s = T_g = T_0$	$x = 0.100 \text{ m} \Rightarrow \begin{cases} -(k_{eff}) \frac{\partial T_s}{\partial x} = \dot{q}_{in}'' \rightarrow 0 \leq t \leq t_h \\ -(k_{eff}) \frac{\partial T_s}{\partial x} = 0 \rightarrow t_h < t \leq t_f \end{cases}$ $x = 0.465 \text{ m} \Rightarrow \begin{cases} -(k_{eff}) \frac{\partial T_s}{\partial x} = 0 \\ -(k_g) \frac{\partial T_g}{\partial x} = 0 \end{cases}$

$$^a Y_{v,0} = \frac{w_{spec,0}}{1+w_{spec,0}} \text{ where } w_{spec,0} = \left(\frac{R_a}{R_v}\right) \left(\frac{P_{v,0}}{P_{a,0}}\right) \text{ and } P_{v,0} = w_{rel,0} P_{sat}(T_0) [8]$$

This system of equations was solved by a one-dimensional numerical model developed in COMSOL Multiphysics. The computational domain mimics the centreline of an experimental apparatus (Fig. 1, Section 2.2). A constant heat flux ( $\dot{q}_{in}''$ ) delivered at the inlet boundary was used to simulate the heater at  $x = 0.1 \text{ m}$ . The Darcy air flux was initiated at  $x=0 \text{ m}$  by a constant  $u_{g,in}$ . A mesh analysis was conducted (Fig. S1, Supplementary Material) and identified that a domain with a 0.1 mm mesh size produced a numerical uncertainty of approximately 1% in the energy balance and 3% in the mass balance. The time-step was varied to meet stability criteria.

A model calibration was conducted along with a global energy balance based on previous studies [54-56] and a new global mass balance was developed (Table 3). Moreover, a model sensitivity analysis was conducted (Runs #1-9, Table 4) where experimental conditions (heater/air on/off) and three model parameters ( $u_g$ ,  $S_w$ ,  $w_{rel}$ ) were changed.

Table 3. Global Energy and Mass Balance

Energy Rate [J s <sup>-1</sup> ]	Eq. #	Global Energy Balance	Mass Flow		
			Rate [kg s <sup>-1</sup> ]	Eq. #	Global Mass Balance
In	24	$\dot{E}_{in} = \dot{q}_{in}'' A_{cs} \big _{x=0.1}$			
Evaporation	25	$\dot{E}_{evap} = \int_{0.1}^{0.465} \Delta H_{evap} \dot{m}_w'''(A_{cs}) dx$	In	30	$\dot{m}_{in} = \rho_{g,in} u_{g,in} A_{cs} \big _{x=0}$
Radial Heat Loss	26	$\dot{E}_{loss} = \int_0^{0.465} -U(2\pi r)(T_s - T_0) dx$	Out	31	$\dot{m}_{out} = \rho_g u_g A_{cs} \big _{x=0.465}$
Out	27	$\dot{E}_{out} = -(\rho_g u_g A_{cs}) C_{p_g} (T_g - T_0) \big _{x=0.465}$			
Net	28	$\dot{E}_{net} = \dot{E}_{in} + \dot{E}_{evap} + \dot{E}_{loss} + \dot{E}_{out}$	Net	32	$\dot{m}_{net} = \dot{m}_{in} - \dot{m}_{out}$

Energy [J]	Eq. #	Global Energy Balance	Mass [kg]	Eq. #	Global Mass Balance
Net	29	$E_{net} = \int_0^{t_f} (\dot{E}_{net}) dt$	Net	33	$m_{net} = \int_0^{t_f} (\dot{m}_{net}) dt$

Table 4. Sensitivity Analysis of Model Parameters

Run # [-]	Heater	Air	$u_g$ [m s <sup>-1</sup> ]	$S_w$ [%]	$w_{rel}$ [%]
1	OFF ( $0 \leq t \leq t_f$ )	ON ( $0 \leq t \leq t_f$ )	0.03	30	10
2	ON ( $0 \leq t \leq t_h$ )	ON ( $0 \leq t \leq t_f$ )	0.05	30	10
3	ON ( $0 \leq t \leq t_f$ )	OFF ( $0 \leq t \leq t_f$ )	-	30	10
4	ON ( $0 \leq t \leq t_h$ )	ON ( $t_g \leq t \leq t_f$ )	0.03	30	10
5	ON ( $0 \leq t \leq t_h$ )	ON ( $t_g \leq t \leq t_f$ )	0.08	30	10
6	ON ( $0 \leq t \leq t_h$ )	ON ( $t_g \leq t \leq t_f$ )	0.05	10	10
7	ON ( $0 \leq t \leq t_h$ )	ON ( $t_g \leq t \leq t_f$ )	0.05	50	10
8	ON ( $0 \leq t \leq t_h$ )	ON ( $t_g \leq t \leq t_f$ )	0.05	30	0
9	ON ( $0 \leq t \leq t_h$ )	ON ( $t_g \leq t \leq t_f$ )	0.05	30	90

## 2.2. Experiments

Three experiments (Table 5) were conducted in a stainless-steel column with 0.160 m inner diameter and 0.505 m in height (Fig. 1). The column was placed over a stainless-steel base (0.14 m inner diameter, 0.20 m in height), containing a flat, spiral-coiled heater (0.14 m outer diameter, 450 W, 120 V, Watlow Ltd) connected to a 120 V AC, single-phase variable power supply (STACO Energy Products), and an air diffuser made of perforated tubes connected to laboratory compressed air supply via a mass flow controller (FMA5400/5500 Series, 0–500 L min<sup>-1</sup>, Omega Ltd). The air diffuser was covered with a 0.10 m layer of commercially available quartz sand (average  $d_p=1.59$  mm, K&E Sand and Gravel, WP #2) up to the top of the heater to ensure uniform airflow.. Then, a 0.20 m layer of wet sand was placed above the heater, topped by a 0.165 m layer of dry sand. Sand was chosen as the porous medium because the convective heat transfer coefficient and thermal properties were well characterized in [39]. Ten thermocouples spaced 0.035 m apart were assumed to measure an average temperature between the solid and gas phases along the column centerline. Data acquisition was set at 2 seconds, which gives enough precision to capture the evolution of the evaporation/condensation fronts. The apparatus was insulated to minimize heat losses. The initial water saturation ( $S_w$ ) was 30 % in the 0.20 m wet layer. The 0.165 m dry layer was introduced to characterize the condensation followed by the evaporation process that is expected to happen as water vapour from the wet area migrates through the reactor.

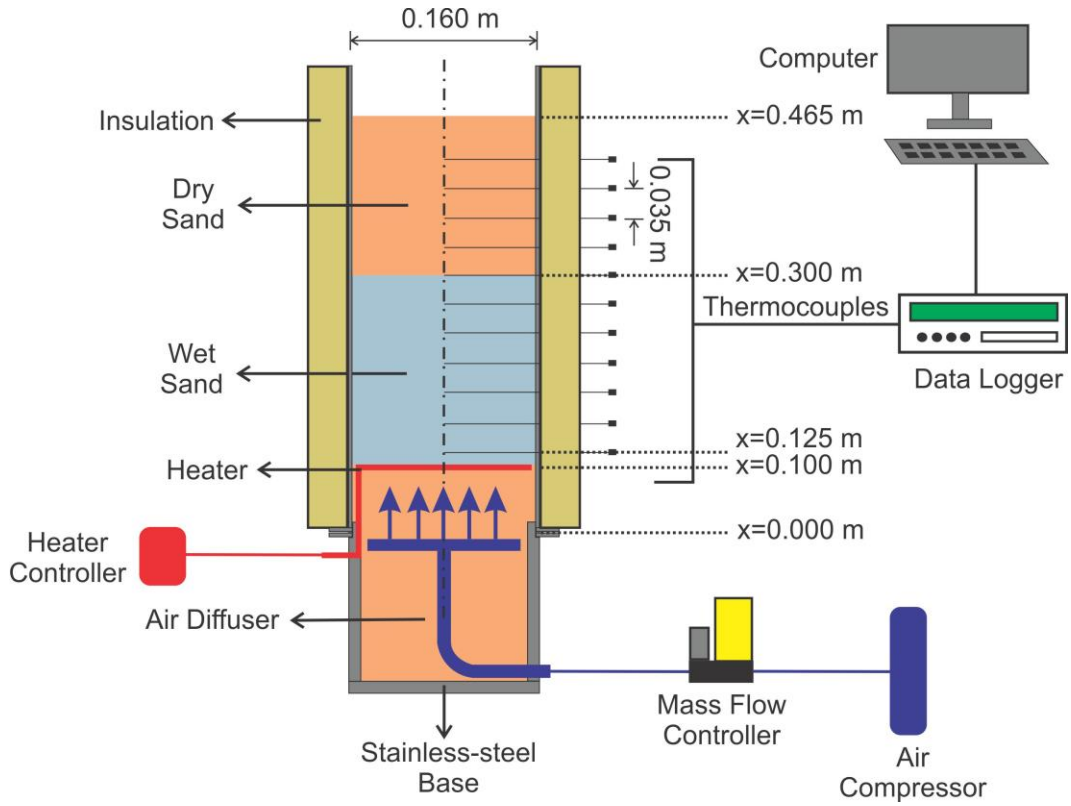


Fig. 1. Schematic of the experimental apparatus for Exp. #2 and #3 (heating). In Exp. #1 (without heating), the column was filled with a 0.465 m layer of wet sand.

Experiment #1 (Table 5) was conducted with the air supply on and heater off, i.e., without heating, until the column was completely dry to observe purely evaporative cooling. Experiments #2 and #3 (Table 5) were initiated by powering the resistive heater until the temperature at the first thermocouple ( $x = 0.125$  m) reached  $250\text{ }^{\circ}\text{C}$ , (Fig. 2b). This creates an initial moisture and temperature gradient within the porous media. Then, air flux ( $u_g$ ), with an initial specific ( $w_{spec,0}$ ) and relative ( $w_{rel,0}$ ) humidity, was supplied at  $t_g$  and the heater was switched off at  $t_h$  while the air was maintained.

Table 5. Water evaporation experiments.

Exp. # [-]	Heater	Air	$u_g$ [ $\text{m s}^{-1}$ ]	$S_w$ [%]	$t_g^a$ [min]	$t_h^b$ [min]
1	OFF ( $0 \leq t \leq t_f$ )	ON ( $0 \leq t \leq t_f$ )	0.03	30	0	-
2 <sup>c</sup>	ON ( $0 \leq t \leq t_h$ )	ON ( $t_g \leq t \leq t_f$ )	0.05	30	70	78
3 <sup>c</sup>	ON ( $0 \leq t \leq t_h$ )	ON ( $t_g \leq t \leq t_f$ )	0.05	30	79	87

<sup>a</sup> time that air flux is turned on; <sup>b</sup> time that heater is turned off; <sup>c</sup> base case



### 3. Results

#### 3.1. Experiments

Figure 2 shows the three experiments described in Table 5. In Fig. 2a, a complex evaporative cooling temperature evolution is shown. Temperatures at all positions drop when air flow was turned on. This is characteristic of evaporative cooling, where air with low relative humidity removes moisture and consequently heat (endothermic process) from the porous medium. A temperature plateau was observed between 12-14 °C, and temperatures stayed constant until approximately 500 min. This plateau will be explained in more detail in the following sections. Then, temperatures drop to approximately 5 °C. After this stage, water was completely removed from the porous medium and temperatures rapidly returned to ambient conditions.

Figure 2b shows the range for two repeats for the heating experiments (Exp. #2 and #3). The experiments start with the heater on and the air supply off. Temperatures increase until the water reaches a boiling plateau at 100 °C. The first thermocouple at  $x = 0.125$  m finished boiling at approximately 50 min, followed by a temperature rise, which indicates that region is dry. The positions above  $x = 0.125$  m were still boiling when the air supply was turned on at approximately 75 min. Temperatures at 0.125 m start to rise due to convective heat transfer from the lower regions [39], while the temperatures at the upper regions drop to approximately 40 °C and stayed relatively constant due to evaporative cooling. When those regions are completely dry, temperatures increase, following the same behaviour of the first thermocouple. The result is a heat wave with decreasing peak temperatures that propagates through the entire column after passing the boiling stage. Note that the heating period was very consistent, varying from 78 to 87 min, since a target temperature (250 °C) was used to end the heating period. This indicates that the experimental repeatability is relatively high. A more detailed explanation of the main processes taking place in Fig. 2 will be presented in the following sections.

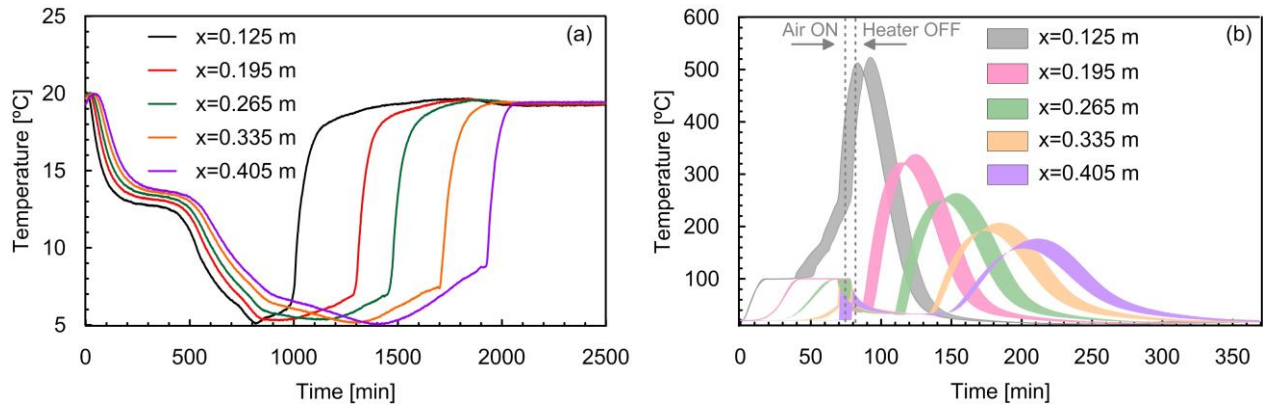


Fig. 2. Experimental temperature evolution versus time for (a) Exp. #1 (without heating) and (b) Exp. #2 and #3 (heating). The coloured shading in (b) encompass the range covered by two experimental repeats (Table 5).

### 3.2. Base Case

#### 3.2.1. Model Calibration

The model was calibrated to the mean behaviour of Exp. #2 and #3 (Table 5), simulating water evaporation during heating conditions. The heating experiments were chosen for the calibration because the heat input adds an additional degree of freedom that is temporally and spatially distributed.

First, the model was tested using literature parameters, i.e., effective thermal properties as described in Eq. (18) and (19), effective diffusivity as shown in Eq. (3), and  $k_{evap} = 1 \text{ s}^{-1}$ . Figure 3 shows that the model can qualitatively reproduce the main features of Exp. #2 and #3.

However, temperatures are shifted in time, which indicates that heat transfer occurs at a slower rate when compared to experimental data. A preliminary analysis identified that the linear averaging used to generate the effective thermal properties (Eq. (18) and (19)) was the main reason for the poor quantitative agreement between experimental data and model-predicted temperatures. This suggests that the presence of water in the porous medium affects  $(k)_{eff}$  and  $(\rho C_p)_{eff}$  in a way that linear averaging cannot capture.

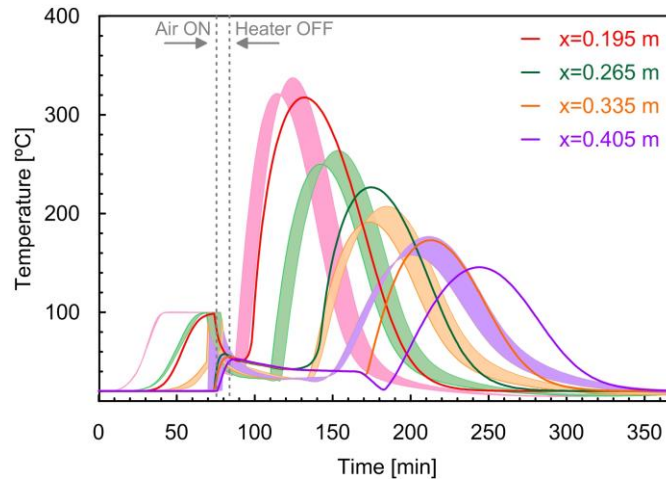


Fig. 3. The coloured shading encompasses two experimental repeats (Exp. #2 and #3) and the solid lines describe average solid and gas model-predicted temperature versus time from 0.195 to 0.405 m with 0.07 m intervals.

Liquid water inside the porous medium creates a “thermal bridge” effect, i.e., a path of least resistance affecting heat transfer differently [58]. Therefore, the effective properties were modified as a function of the sand and water thermal properties:

$$(k)_{eff} = (\delta)((1 - \phi)(k_s + k_{rad}) + (\phi S_w)k_w) \quad (23)$$

$$(\rho C_p)_{eff} = (\gamma)((1 - \phi)\rho_s C_{ps} + (\phi S_w)\rho_w C_{pw}) \quad (24)$$

Two sensitivity constants,  $\gamma$  and  $\delta$ , were introduced to analyse the sensitivity of liquid water on the effective properties. While  $\gamma$  and  $\delta$  do not represent independent physical processes, they allow quantification of variability without needing to resolve what a stochastic effect is.  $\gamma$  and  $\delta$  were varied from 0.6 to 1.8. Figures 4a,b reveal that a decrease in  $(\rho C_p)_{eff}$  to  $\gamma = 0.6$  results in faster heat propagation due to an increase in the thermal diffusivity i.e.,  $\alpha = (k)_{eff} / (\rho C_p)_{eff}$  (Fig. 4c). Similar behaviour was observed when  $k_{eff}$  was increased ( $\delta = 1.8$ ) (Fig. 4d,e). However, although  $\alpha$  was altered by the same magnitude (Fig. 4c and 4f),  $(\rho C_p)_{eff}$  was observed to have the highest impact on the temperature curves. This is because  $(\rho C_p)_{eff}$  represents the capacity of the medium to store and release energy, i.e., a low  $(\rho C_p)_{eff}$  indicates that energy is quickly released to the surroundings, resulting in high peak temperature and fast heat transfer propagation. Similar behaviour occurs with a high  $k_{eff}$ , which conducts heat much faster, however, leading to more local heat losses (low peak temperature). In forced air conditions, heat

transfer is dominated by convection [39], decreasing the effects of  $k_{eff}$ . Note that  $\alpha$  shows a relatively weak linear relationship for  $(\rho C_p)_{eff}$  ( $R^2 = 0.91$ , Fig. 4c) and a strong linear relationship for  $k_{eff}$  ( $R^2 = 1$ , Fig. 4f).

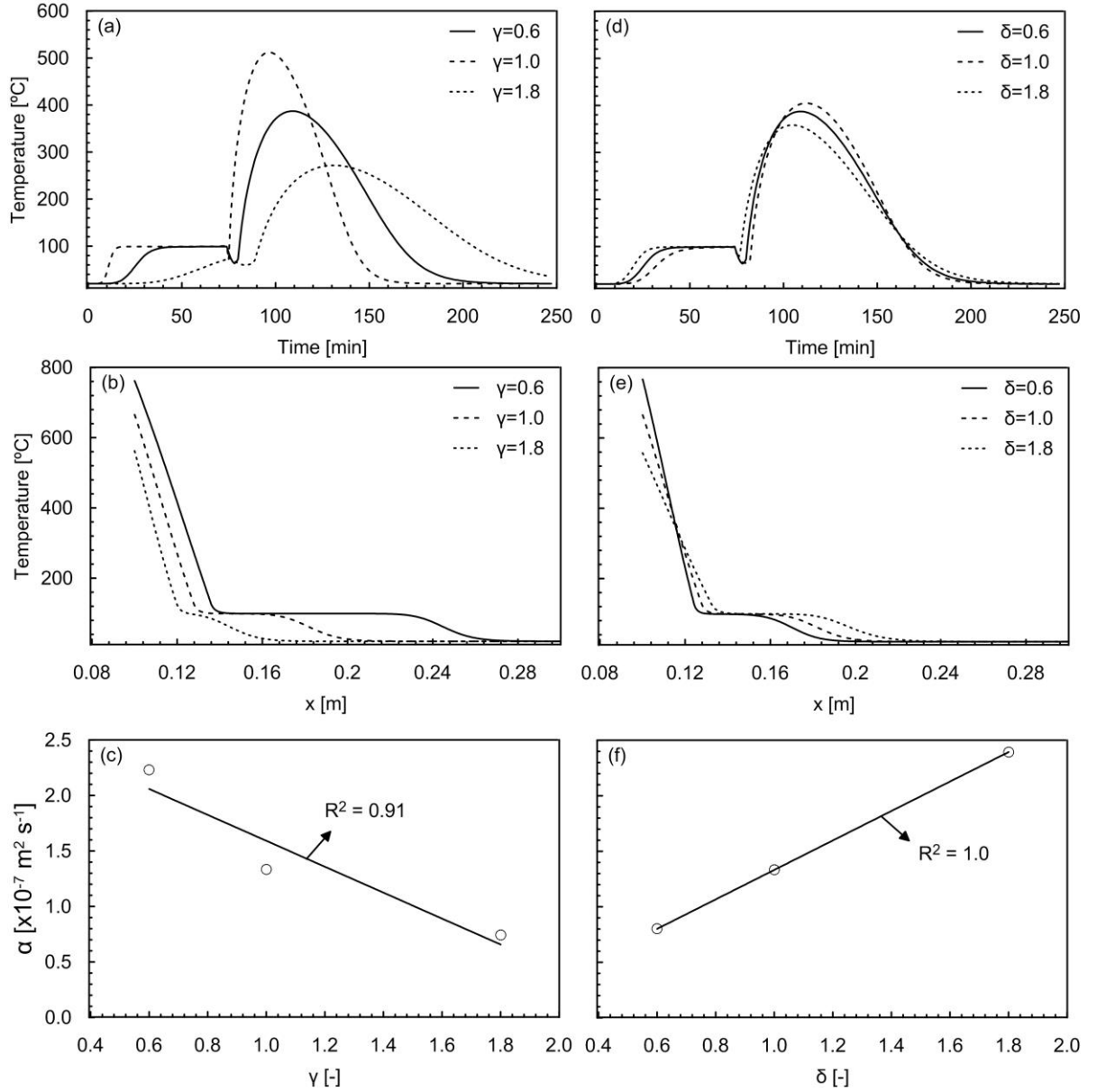


Fig. 4. Sensitivity analysis showing the model-predicted average temperature in (a,d) time and (b,e) space depicted at  $x = 0.16$  m and  $t=43$  min (position and time at which heater is on and air is off) for  $\gamma$  and  $\delta$ . Thermal diffusivity ( $\alpha$ ) for (c)  $\gamma$  and (d)  $\delta$ .

Moreover, a sensitivity analysis of  $D_{eff}$  and  $k_{evap}$  was conducted (Fig. 5). Previous studies suggest that  $D_{eff}$  usually varies from  $10^{-4}$  [49] to  $10^{-5}$  m<sup>2</sup>/s [8, 42, 53], whereas  $k_{evap}$  is a process-dependent variable and it has a wide applicability range ( $k_{evap} < 10^6$  s<sup>-1</sup> [11, 13]). The sensitivity analysis revealed that  $D_{eff}$  affects the temperature plateau and the rate that temperature increases below 100 °C (Fig. 5a,b). Large  $D_{eff}$  values result in a slow temperature increase (lower condensation rates, see Section 3.3 for details) because water vapor is more likely to diffuse into the air rather than condense in the upper regions. In general, the influence of  $D_{eff}$  on the evaporation process is local and has higher effects during non-convection conditions (i.e., before air injection), with a negligible impact on the forced air evaporation process. This observation is also supported by the constant thermal diffusivity  $\alpha$  in Fig. 5c.

Figures 5d,e show that a high  $k_{evap}$  increases the evaporation rate, slightly changing the temperature plateau and rapidly decreasing the temperature around 80 min when air is turned on (further details Section 3.3) since more energy is removed from the system due to endothermic evaporation. However, the overall impact of  $k_{evap}$  on the temperature is relatively small (constant  $\alpha$ , Fig. 5f) and equilibrium mass transfer (i.e., negligible changes in temperature and evaporation/condensation rates) is reached for  $k_{evap} > 5$  s<sup>-1</sup>.

Therefore, based on this sensitivity analysis, four model parameters ( $\gamma$ ,  $\delta$ ,  $D_{eff}$ , and  $k_{evap}$ , Table 1) were calibrated mimicking the conditions of Exp. #2 and 3 (Table 5) and the results are presented in Fig. 6a, Section 3.2.2. Note that the calibrated value  $\gamma = 0.7$  may result in a  $(\rho C_p)_{eff}$  less than the porosity-averaged  $\rho C_p$  for sand alone. As indicated above, this is due to the effective approach to the thermal properties used through the calibration constants. The phenomena that are not described can include: i) unknown temperature effects on the  $C_p$  for a water saturated porous medium, ii) unknown water effects on the effective thermal properties, iii) unknown changes in the system thermal diffusivity that are corrected by a lower  $\rho C_p$ .

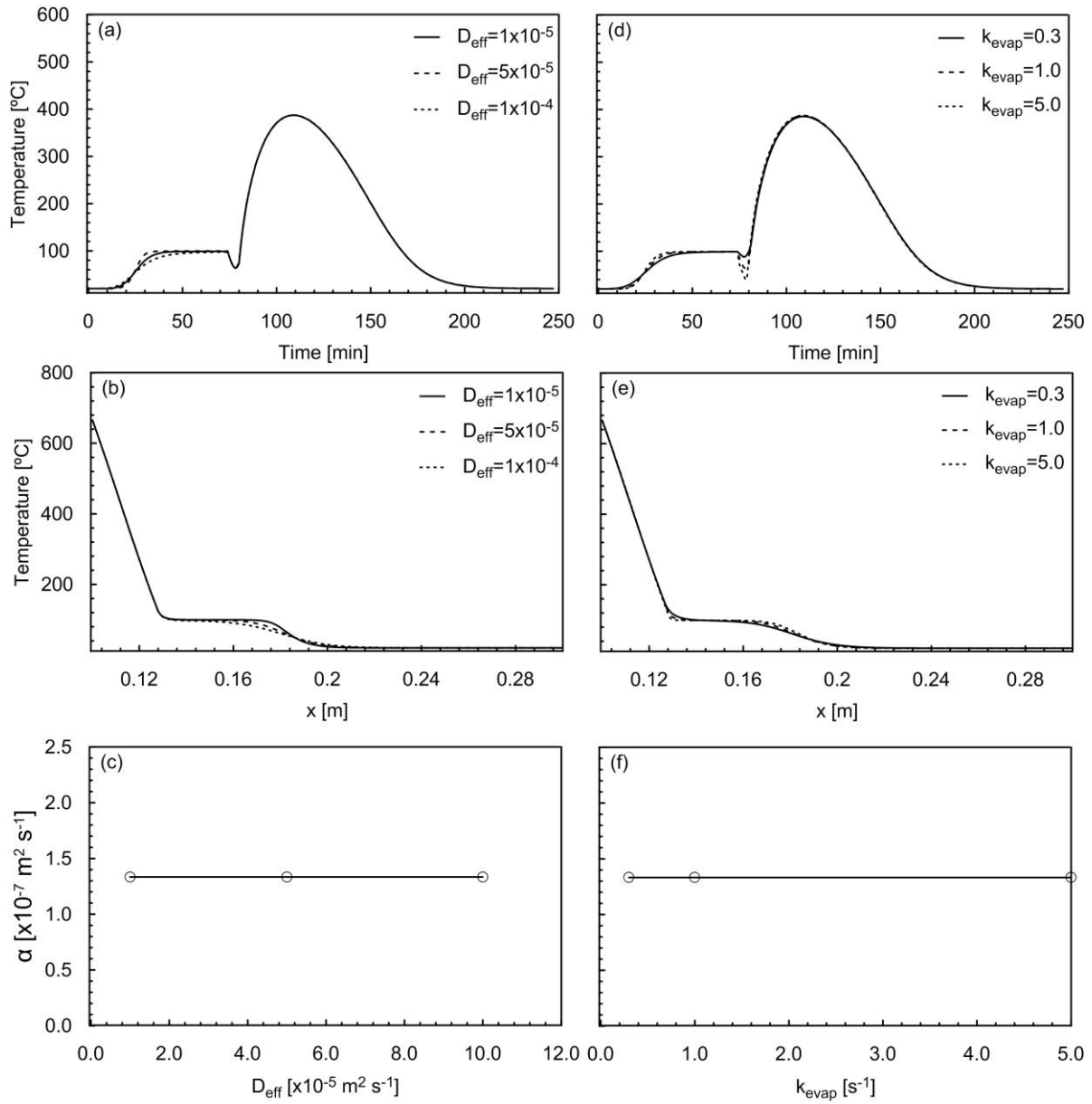


Fig. 5. Sensitivity analysis showing the model-predicted average temperature in (a,d) time and (b,e) space depicted at  $x = 0.16$  m and  $t = 43$  min for  $D_{eff}$  (m<sup>2</sup> s<sup>-1</sup>) and  $k_{evap}$  (s<sup>-1</sup>). Thermal diffusivity  $\alpha$  for (c)  $D_{eff}$  (m<sup>2</sup> s<sup>-1</sup>) and (d)  $k_{evap}$  (s<sup>-1</sup>).

### 3.2.2. Evaporation and Condensation

Figure 6a shows that the calibrated model well predicts experimental temperatures with average 8% difference. This difference is mostly found in the temperature curves preceding the temperature plateau and during cooling stage.. However, this is likely related to the simple approach used for the evaporation

rate, effective thermal properties, and effective diffusivity (see Section 3.2.1). Figure 6a shows that during the ‘heater on’ and ‘air off’ period, i.e.,  $(0 \leq t \leq t_h)$  and  $(0 \leq t < t_g)$ , a temperature plateau at 100 °C is reached at 0.195 m. At 35 min, this plateau has a length of 12 cm (Fig. 6a) and can be explained by the occurrence of several simultaneous processes. The region near the heater ( $x = 0.10$  m, see Fig. S4, Supplementary Material) is primarily affected by high temperatures. Thus, the rate of water evaporation is instantaneous, water saturation rapidly decreases because  $P_v \ll P_{sat}$  [11, 13] and the temperature plateau is absent. Similar behaviour was found during low water saturations [12, 15].

Then, the water vapour produced during evaporation, moves to the upper regions (see increase in the vapour mass fraction in Fig. 5b and increase in  $u_g$  during ‘air off’ period, Fig. 6c and Fig. 7b), and since  $P_v$  is slightly higher than  $P_{sat}$  (Fig. 6d), vapour condenses in the cold regions above [15]. This water vapour condensation results in an increase in water saturation (e.g.,  $x = 0.195$  m, Fig. 6e and at 35 min in Fig. 7c), represented by a positive peak (Fig. 6f and Fig. 7d) in the evaporation rate, and relative humidity higher than 100% (Fig. 6g). Note that, the condensation region (e.g., positive peak in Fig. 7d at 35 min) is relatively large (~5 cm). Finally, vapour condensation releases heat into the porous medium, increasing the temperature at that region. The experimental temperature at  $x=0.195$  m reaches the boiling plateau (100 °C) at approximately 35 min and remains relatively constant until 70 min. The numerical temperature stabilizes at approximately 98.5 °C (see details in Fig. S5, Supplementary Material). It is important to note that the numerical temperature ‘plateau’ is not actually representing boiling, because: i) Eq. (14) is based on a non-equilibrium approach, i.e., it cannot simulate boiling, which by definition represents a thermodynamic equilibrium ( $P_v = P_{sat}$ ) and ii) the vapour pressure is slightly higher than the water saturation pressure ( $P_v > P_{sat}$ ), which indicates that condensation takes place during the temperature plateau. This can be observed in Fig. 6e, where the water saturation slightly increases at the plateau. A zoom-in shows that the numerical temperature is slightly increasing between 35-70 min, but at a very slow rate. To explain this behaviour, the regions below  $x=0.195$  m will be used as an example (details in Fig. S6, Supplementary Material). At  $x=0.145$  m, evaporation is occurring and all the energy in the system is used to evaporate water via the heat of vaporization ( $\Delta H_{vap}$ ), agreeing with [12]. Therefore, there is no energy being propagated upwards, and the temperature at  $x=0.155$  m slightly increases only due to the energy released by condensation. Evaporation is only activated at  $x=0.155$  m when the region at  $x=0.145$  m is completely dry. Then, temperature in that region increases above 100 °C, energy is propagated upwards, activating evaporation at  $x=0.155$  m. Similar behaviour was found in [12].

During the period of ‘heater off’ and ‘air on’, i.e.,  $(t_h \leq t \leq t_f)$  and  $(t_g \leq t < t_f)$ , a rapid temperature decrease is observed (Fig. 6a) due to evaporative cooling. Water saturation decreases (i.e., liquid water becomes

vapour) due to a strong thermodynamic disequilibrium (Fig. 6e), caused by a decrease in the vapour pressure below the water saturation pressure, i.e.,  $P_v < P_{sat}$ , resulting in a large negative peak in the evaporation rate (Fig. 6f). Moreover, this causes a decrease in the vapour mass fraction (Fig. 6b), i.e., vapour is carried forward much faster and does not accumulate in that region. Note that, at 105 min, evaporative cooling (negative peak in Fig. 7d) is concentrated in a much thinner region (~1.5 cm) when compared to condensation. Relative humidity ( $w_{rel}$ ) increases and is higher than 100% (Fig. 6g), due to all the water that is evaporated and transferred to the gas phase as vapour. Later, it decreases because vapour moves upwards with the air and then returns to ambient relative humidity conditions since fresh air flows through a now ‘dry’ region. As a result, the total gas pressure decreases, and temperatures stabilize at 50-60 °C, agreeing with [15]. Evaporative cooling will be explained in detail in Section 3.3.

Water vapour travels upwards condensing in the initially ‘dry layer’ of the column ( $x > 0.3$  m). Figure 6e shows this phenomenon, where water saturation is originally zero in the ‘dry layer’ and then increases due to vapour condensation (positive peak in the evaporation rate, Fig. 6f). When the heat wave reaches that region, water evaporation occurs (decrease in water saturation, Fig. 6e), and is represented by a negative peak in the evaporation rate, Fig. 6f, with a decrease in the temperature curve at  $x = 0.405$  m (Fig. 6a, ~150 min) due to energy removal. Additional supporting data for this analysis is provided in the Supplementary Material.



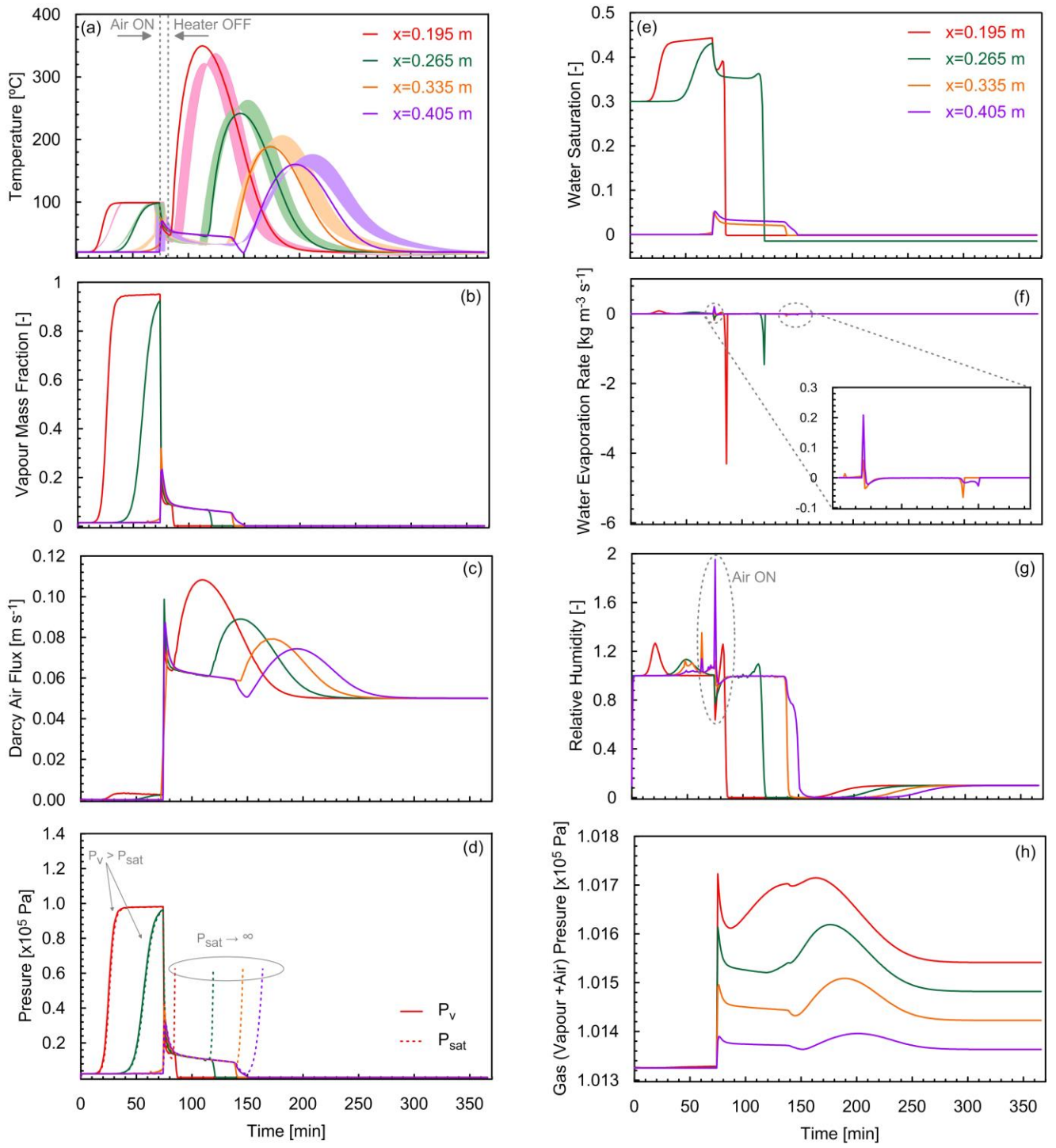


Fig. 6. Solid lines describe (a) average solid and gas model-predicted temperature and (b-h) the model-predicted variables versus time from 0.195 to 0.405 m with 0.07 m intervals. (a) The coloured shading encompasses two experimental repeats (Exp. #2 and #3).

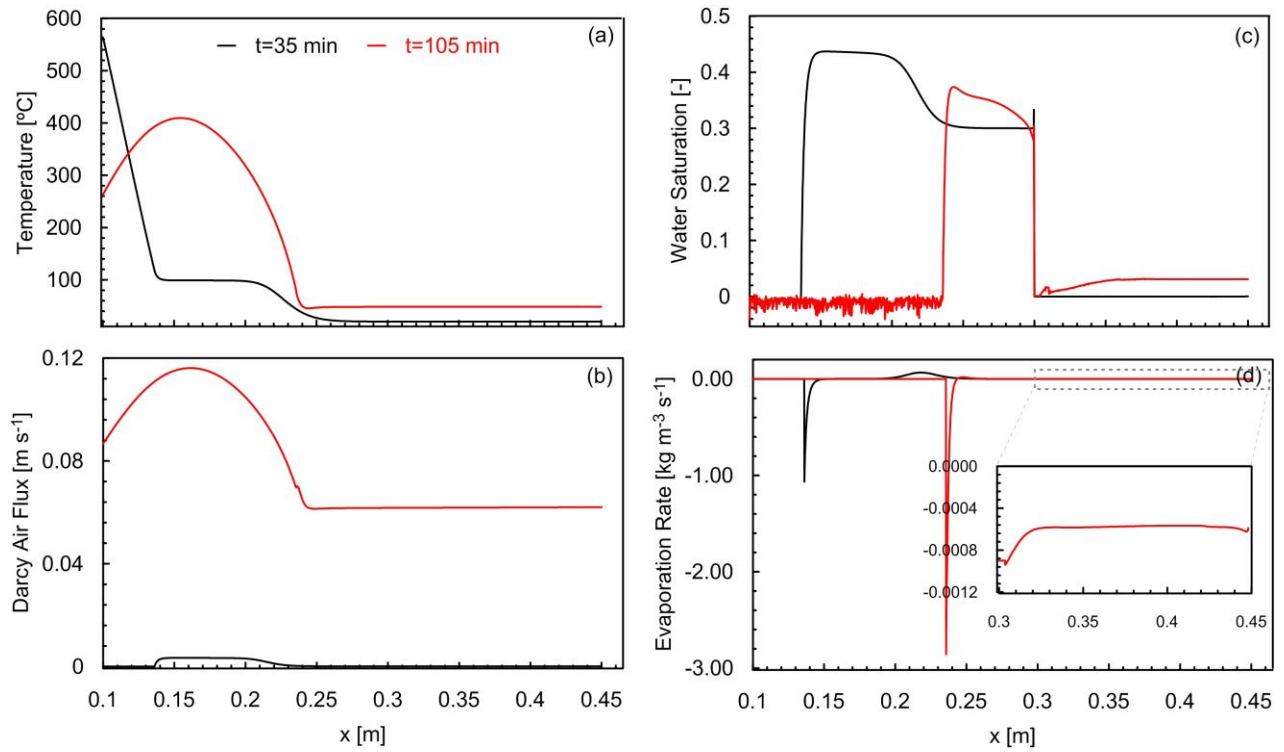


Fig. 7. Solid lines describe the model-predicted variables versus column height ( $x$ ) for base case at two depicted times: 35 min and 105 min.

### 3.2.3. *LTE vs LTNE*

A comparison of simulated results using LTE versus LTNE during water evaporation and condensation for base case (Exp. #2 and #3, Table 5) is presented in Fig. 8. Figure 8a shows that temperatures of the gas and solid phases are in LTE when air is not supplied as a result of the assumption of a high  $h_{sg}$  (see Section 2.2). When air supply is turned on, LTNE between solid and gas phases via Eq. (22) is significant in the wet region, associated with an average temperature difference of 27% (Fig. 8b). Figure 7b also shows that in the dry region, the average temperature difference drops to 7%, which agrees with the values found in [39] for heated sand without water. This indicates that the presence of water alters the energy balance (see Section 3.3), resulting in LTNE between the solid and gas phases. Moreover, gas temperature is hotter than solid temperature due to *i*) water evaporation in the solid phase, which decreases its temperature (see sharp decrease between 80 min and 90 min) and *ii*) the addition of hot vapour into the gas phase, increasing its temperature. When LTE is assumed, i.e.,  $T_g = T_s = T$ , Eqs. (16) and (17) are combined, and the result is an overestimation of the peak temperature and too rapid predicted temperature cooling.

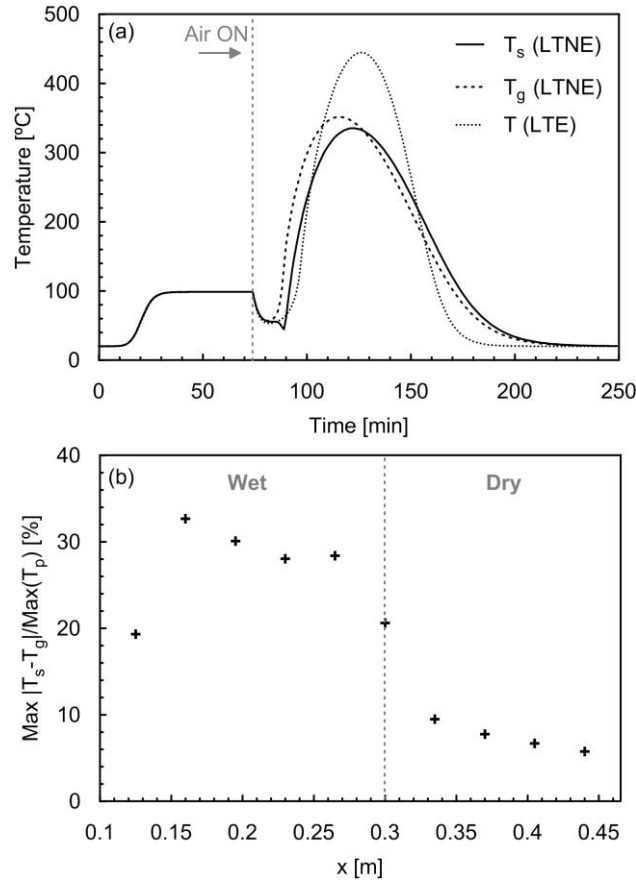


Fig. 8. (a) Simulated solid ( $T_s$ ) and gas ( $T_g$ ) temperature in LTNE and simulated temperature ( $T$ ) in LTE at  $x = 0.195$  m for base case. (b) Maximum simulated  $T_s$  and  $T_g$  normalized by the maximum peak temperature ( $T_p$ ) varying with column height ( $x$ ).

#### 3.2.4. Global Energy Balance

Figure 9 shows the global energy balance for the base case (Exp. #2 and #3, Table 5). When the air supply is off, the net energy rate ( $\dot{E}_{net}$ ) is positive due to the constant energy rate supplied by the heater ( $\dot{E}_{in}$ ) but decreases with time because of an increase in the lateral losses ( $\dot{E}_{loss}$ ) as the temperature of porous media increases (Fig. 9b). The energy rate for evaporation-condensation ( $\dot{E}_{evap}$ ) is negligible during this time-period, since it is governed by a balance between energy absorbed by evaporation and released by condensation in the upper regions. Note that the energy rate at the outlet ( $\dot{E}_{out}$ ) is also zero, which indicates that no energy is leaving at the outlet, i.e., water vapour created during evaporation is condensing upwards, resulting in a relatively constant mass loss (Fig. S7a). This results in a net energy ( $E_{net}$ ) increasing with time, due to the energy stored in the porous medium, Fig. 9c.

When the air supply is turned on,  $\dot{E}_{evap}$  abruptly drops to negative values due to evaporative cooling, followed by a decrease in  $\dot{E}_{out}$ , which indicates that water vapour is leaving the system (Fig. 9b and Fig. S7a). This is confirmed by a decrease in both  $E_{net}$  (Fig. 9c) and mass loss. When  $\dot{E}_{in}$  is turned off,  $\dot{E}_{net}$  decreases to negative values (Fig. 9c) dominated by  $\dot{E}_{evap}$ ,  $\dot{E}_{loss}$ , and  $\dot{E}_{out}$ . At approximately 150 min,  $E_{net}$  reaches a plateau (Fig. 9c) due to vapour condensation in the dry region, and then decreases because of evaporative cooling (sharp decrease in temperature at  $x=0.405$  m). Then, energy leaves the system by lateral losses via  $\dot{E}_{loss}$  (becoming less negative due to cooler temperatures) and by  $\dot{E}_{out}$  (negatively increasing due to water leaving at the outlet) until ambient conditions. Further data that support this analysis is provided in the Supplementary Material.

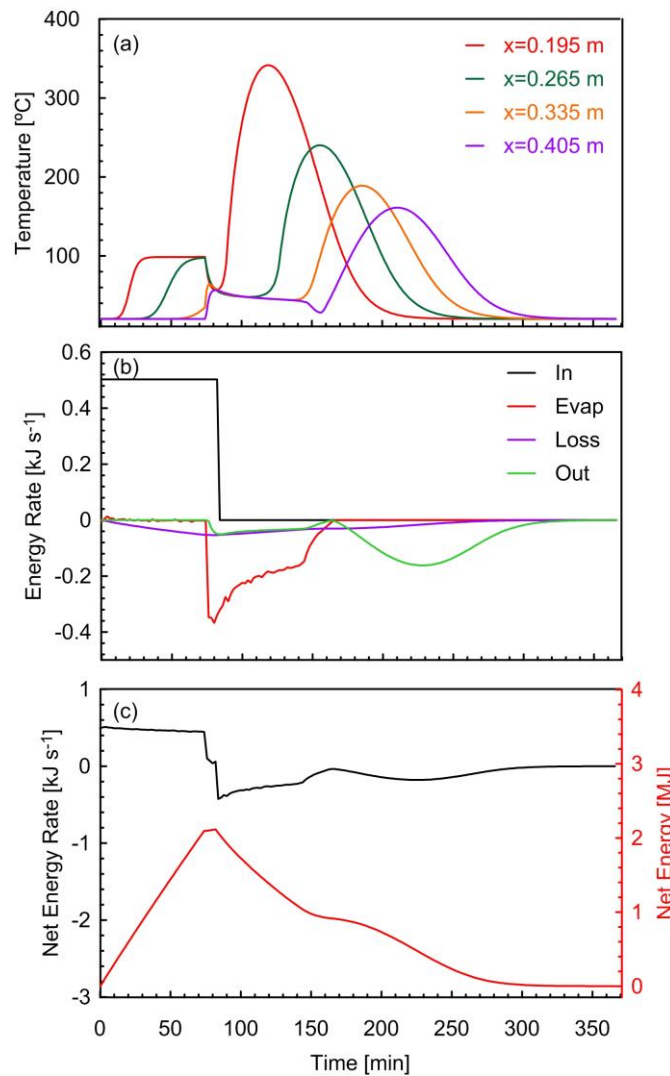


Fig. 9. (a) Base case model-predicted average gas and solid temperature, (b) Global energy rate for each component (Table 3, Eqs. (23-28)), and (c) Global net energy rate and global net energy versus time (Table 3, Eqs. (29) and (32)).

### 3.3. Evaporative Cooling

#### 3.3.1. No Heating

An experiment with no heating is used to establish the capability of the calibrated model to reproduce the experimental results. Figure 10 shows a comparison between Exp. #1 (Table 5) and the model-predicted temperature under evaporative cooling conditions (Run #1, Table 4), i.e., evaporation is due to ambient air with low relative humidity flowing through the porous medium without heating. The parameters calibrated in Section 3.2.1 and shown in Table 1 were used here, i.e., no additional calibration was conducted. The model was able to qualitatively predict most of the experimental trends. A sensitivity analysis of the parameters calibrated in Section 3.2.1 was conducted to identify the possible reasons for the quantitative mismatch between experimental and numerical data (Fig. 11). The sensitivity revealed that at low temperatures,  $(k)_{eff}$  has a higher effect on the temperature (Fig. 11b) than  $(\rho C_p)_{eff}$  (Fig. 11b), contrary to high temperature heating experiments (Fig. 4). Moreover, changes in  $(k)_{eff}$  vertically shifts the temperature plateau, which might be further evidence of the “thermal bridge” effect caused by water within the porous. Figure 11 also shows that lower  $k_{evap}$  values create a larger temperature plateau (Fig. 11c), similar to the experiment, which indicates that during evaporative cooling without heating water evaporation occurs at a slower rate than with heating. Finally, an increase in the relative humidity of air did not result in significant temperature decreases, as expected, due to minimal evaporation since the air is already saturated with moisture. Note that an analysis of the effective diffusivity indicated no effect on the temperature trends (not shown).

Figure 12 shows that when air flow is turned on, evaporative cooling rapidly decreases the temperature along the entire system (Fig. 12a). This is confirmed by a slight decrease in water saturation (Fig. 12b), a negative peak in the evaporation rate (Fig. 12c), and a decrease in relative humidity (Fig. 12d), vapour mass fraction (Fig. 12e), and air flux (Fig. 12f) during the first 200 min. At this stage,  $P_v$  is lower than  $P_{sat}$  (Fig. 12g) and the total pressure slightly decreases (Fig. 12h). Then, a temperature plateau is created (Fig. 12a) because  $w_{rel}$  is close to 1 and  $P_v$  approaches to  $P_{sat}$ , but it is still slightly lower. Thus, evaporation slows down, and the temperature stabilizes for up to 100 min. When  $w_{rel} < 1$ , water evaporation is re-initiated, i.e.,  $S_w$  decreases (Fig. 12b) and the evaporation rate peaks (Fig. 12c). Temperature in each specific location decreases until all the water is removed, and then returns to ambient conditions.

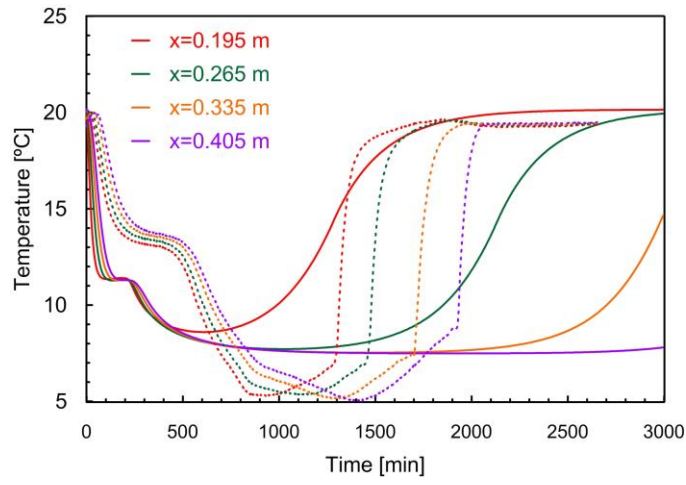


Fig. 10. Solid lines describe the model-predicted average gas and solid temperature versus time from 0.195 to 0.405 m with 0.07 m intervals. The dashed lines represent Exp. #1.

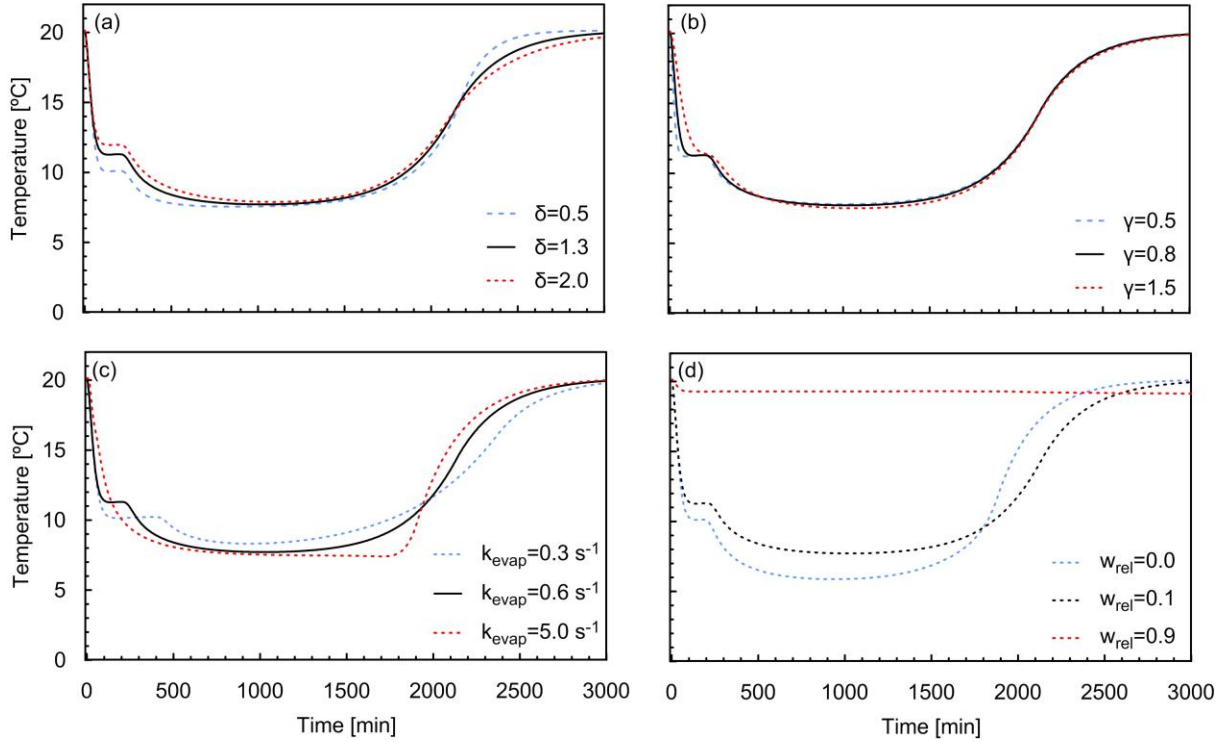


Fig. 11. Sensitivity analysis showing the model-predicted average sand and gas temperature for Exp. #1 depicted at  $x = 0.265$  m for  $\delta$ ,  $\gamma$ ,  $k_{evap}$ , and  $w_{rel}$ .

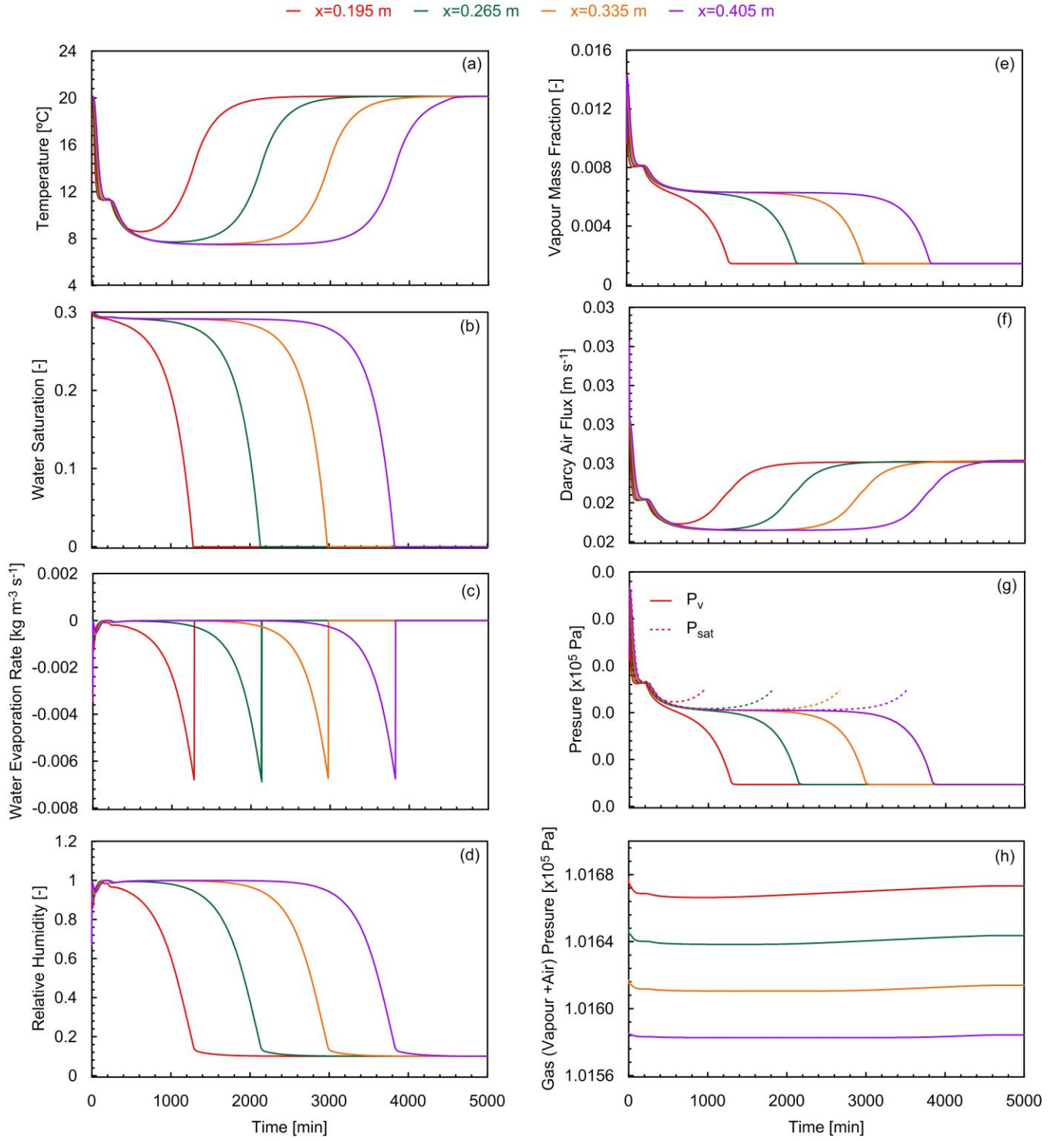


Fig. 12. Model-predicted variables versus time for Exp. #1 from 0.195 to 0.405 m with 0.07 m intervals.



### 3.3.2. Heating

Figure 13 shows evaporative cooling under heating conditions. Runs #2 and #3 (Table 4) will be used to explain this behaviour. In Run #2, the air flow and the heater are on from  $t = 0$  min, while in Run #3, the heater was kept on and the air flow was kept off during the entire simulation ( $0 \leq t \leq t_f$ ). Run #2 shows a temperature ‘plateau’ around 50 °C. This behaviour has been seen several times in the smouldering literature [59] during convective ignition. Evaporation occurs in the lower regions and the created vapour moves upwards and condenses in the upper regions, since  $P_v > P_{sat}$  (Fig. 13b). However, condensation is not very significant, when compared to the “air off” case (Fig. S9e), since more vapour leaves the system in the gas phase. Consequently,  $P_v$  decreases to relatively low values. Less condensation results in less energy released into the system, increasing the temperature only up to 50 °C. For Run #3 (“air off” case), the temperature increase is approximately 50% higher, i.e., 98.5 °C (Fig. 13c), and evaporative cooling does not occur. In both cases, the temperature ‘plateau’ is formed because of all the energy available is used to evaporate water, as explained in Section 3.2.2. Further details are provided in Fig. S8 and S9 (Supplementary Material).

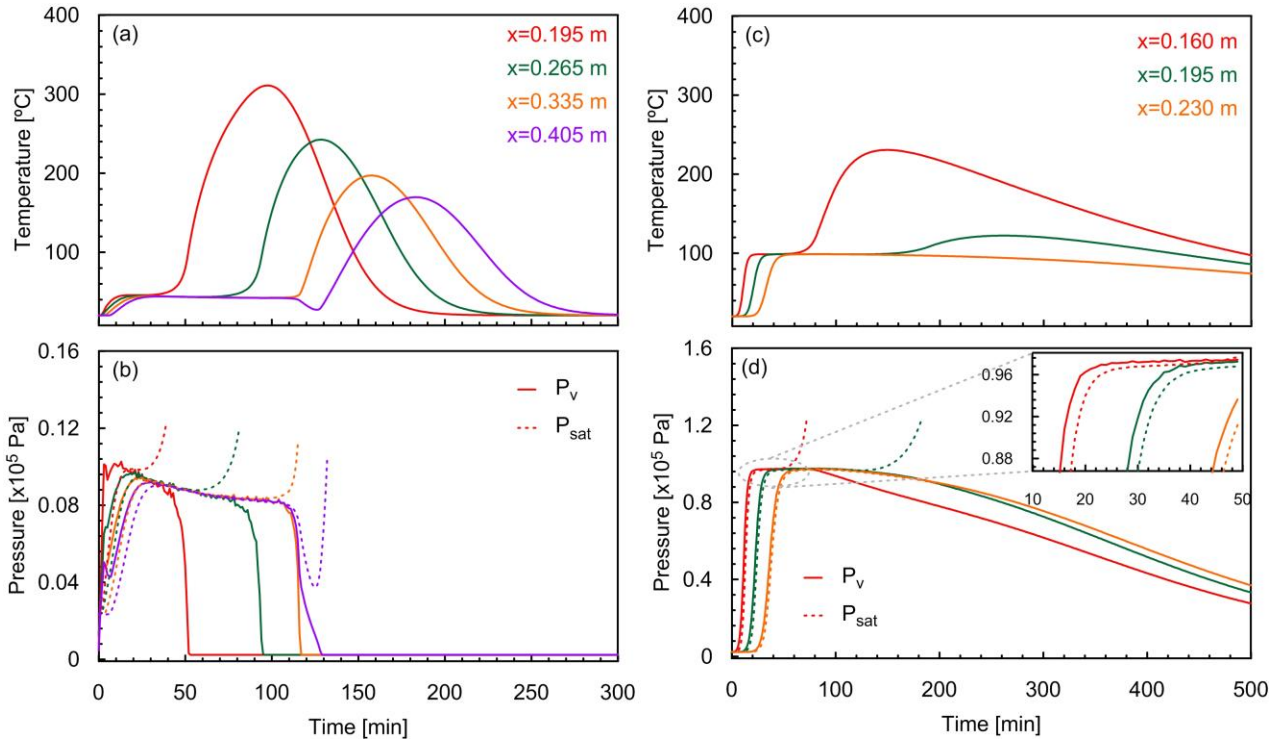


Fig. 13. Average sand and gas temperature, vapour pressure ( $P_v$ ) and saturation pressure ( $P_{sat}$ ) for (a, b) Run #2 and (c, d) Run #3.



### 3.4. Sensitivity Analysis of $u_g$ , $S_w$ , $w_{rel}$

A sensitivity analysis was conducted (Run #4-9, Table 4) to simulate changes in the experimental conditions, such as air flux ( $u_g$ ), water saturation ( $S_w$ ) and air supply relative humidity ( $w_{rel}$ ), Fig. 14. The analysis revealed that an increase in  $u_g$  does not affect the temperature plateau as expected since air is off. However, when air is on, convective heat transfer results in high peak temperatures and fast cooling (Fig. 14a). In contrast, an increase in  $S_w$  increases the length of the temperature plateau (Fig. 14b) since it takes more time to evaporate water [38]. Moreover, the rate of temperature increase is much faster for high saturations because of water condensation (see Section 3.2.2). An increase in  $S_w$  also decreases the peak temperature because of more energy being removed from the system and not carried forward by the air flow. Finally, the sensitivity showed that  $w_{rel}$  does not affect the temperature profiles (Fig. 14c), but there is less vapour going into the gas phase. Further details are presented in Fig. S10-S15, Supplementary Material.

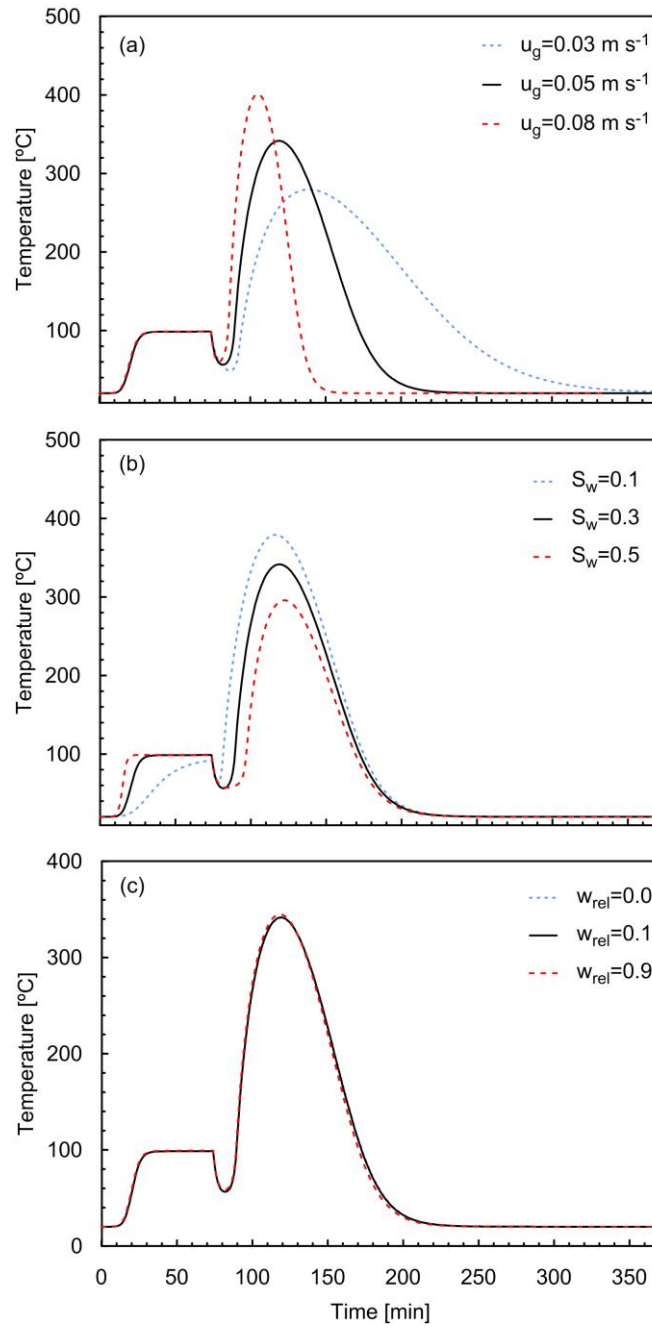


Fig. 14. Model-average sand and gas temperature at  $x=0.195$  m varying with air flux ( $u_g$ ), water saturation ( $S_w$ ) and relative humidity of air supply ( $w_{rel}$ ).

#### 4. Conclusions

A numerical model was constructed to predict the transient and spatial resolution of the progression of one-dimensional evaporation and condensation fronts in a porous media partially saturated with water. The model included a comprehensive representation of transport processes in the gas phase as well as evaporation and condensation models. The model simplified the impact of water saturation on the thermal properties by means of effective properties obtained through a linear average of the sand and water properties weighted by the saturation. The comparison between the numerical and experimental results indicated that this linear average was insufficient to describe the complex heat transfer mechanisms between water and sand. The results showed that by introducing simple calibration constants, the model was able to accurately predict experimental results for a wide range of conditions independent of the tests used for calibration. Furthermore, the calibrated model allowed to understand and then was able to describe and characterize a multiplicity of additional physical processes.

During heating and air-off conditions, a temperature plateau representing the phase-change process was accurately simulated, agreeing with the experiment. This temperature plateau was caused by condensation of water vapour transported from the regions near the heater. Therefore, there was no upward energy propagation due to conduction and radiation, since all the available energy was used to evaporate water near the heater. When evaporation was terminated and the region was dried, energy was transferred upwards by heat transfer mechanisms, and temperatures increased above 100 °C. During heating and air-on conditions, the model was also able to accurately predict evaporative cooling, resulting in a rapid temperature decrease until stabilizes at 50-60 °C, agreeing with the experiment. This was caused because vapour was carried forward much faster by the forced air, resulting in lower condensation and consequently lower energy released.

Local thermal non-equilibrium between solid and gas phases was significant in the wet region, creating an average of 27% temperature difference, whereas the average temperature difference in the initially dry region was 7%. This indicated that the energy balance was altered during water evaporation and condensation and local thermal non-equilibrium conditions need to be assumed. Finally, a sensitivity analysis revealed that an increase in the water saturation increases the length of the temperature plateau since it takes more time to evaporate water and decreases the peak temperature because of more energy removed from the system. This work provided unique conclusions about evaporative cooling and water evaporation and condensation in space and time and will be the basis for simulating such processes in complex systems such as smouldering combustion of wet fuels.

## Acknowledgements

Funding was provided by the Natural Sciences and Engineering Research Council of Canada to the fourth author.

## References

- [1] B. Peters, E. Schröder, C. Bruch, T. Nussbaumer, Measurements and particle resolved modelling of heat-up and drying of a packed bed, *Biomass and Bioenergy*, 23 (2002) 291-306.
- [2] Z.H. Wang, G. Chen, Heat and mass transfer in fixed-bed drying, *Chemical Engineering Science*, 54 (1999) 4233-4243.
- [3] A.C. Trautz, K.M. Smits, A. Cihan, Continuum-scale investigation of evaporation from bare soil under different boundary and initial conditions: An evaluation of nonequilibrium phase change, *Water Resources Research*, 51 (2015) 7630-7648.
- [4] E. Ballarini, B. Graupner, S. Bauer, Thermal–hydraulic–mechanical behavior of bentonite and sand-bentonite materials as seal for a nuclear waste repository: Numerical simulation of column experiments, *Applied Clay Science*, 135 (2017) 289-299.
- [5] J. Bruining, A.A. Mailybaev, D. Marchesin, FILTRATION COMBUSTION IN WET POROUS MEDIUM, *SIAM Journal on Applied Mathematics*, 70 (2009) 1157-1177.
- [6] M.A. Bazelat Zononi, H. Massard, M. Ferreira Martins, Formulating and optimizing a combustion pathways for oil shale and its semi-coke, *Combustion and Flame*, 159 (2012) 3224-3234.
- [7] A. Halder, A. Dhall, A.K. Datta, Modeling Transport in Porous Media With Phase Change: Applications to Food Processing, *Journal of Heat Transfer*, 133 (2010).
- [8] F.A. Khan, C. Fischer, A.G. Straatman, Numerical model for non-equilibrium heat and mass exchange in conjugate fluid/solid/porous domains with application to evaporative cooling and drying, *International Journal of Heat and Mass Transfer*, 80 (2015) 513-528.
- [9] M.R. Assari, H. Basirat Tabrizi, M. Saffar-Avval, Numerical simulation of fluid bed drying based on two-fluid model and experimental validation, *Applied Thermal Engineering*, 27 (2007) 422-429.
- [10] M. Izadifar, O.-D. Baik, C.J. Simonson, Modeling of the packed bed drying of paddy rice using the local volume averaging (LVA) approach, *Food Research International*, 39 (2006) 712-720.
- [11] C. Kumar, M.U.H. Joardder, T.W. Farrell, G.J. Millar, A. Karim, A porous media transport model for apple drying, *Biosystems Engineering*, 176 (2018) 12-25.
- [12] E. Purlis, Modelling convective drying of foods: A multiphase porous media model considering heat of sorption, *Journal of Food Engineering*, 263 (2019) 132-146.

- [13] M.U.H. Joardder, C. Kumar, M.A. Karim, Multiphase transfer model for intermittent microwave-convective drying of food: Considering shrinkage and pore evolution, *International Journal of Multiphase Flow*, 95 (2017) 101-119.
- [14] G.H.A. van der Heijden, R.M.W. van Bijnen, L. Pel, H.P. Huinink, Moisture transport in heated concrete, as studied by NMR, and its consequences for fire spalling, *Cement and Concrete Research*, 37 (2007) 894-901.
- [15] C. Di Blasi, Multi-phase moisture transfer in the high-temperature drying of wood particles, *Chemical Engineering Science*, 53 (1998) 353-366.
- [16] X. Huang, G. Rein, Upward-and-downward spread of smoldering peat fire, *Proceedings of the Combustion Institute*, 37 (2019) 4025-4033.
- [17] L. Yermán, H. Wall, J.L. Torero, Experimental investigation on the destruction rates of organic waste with high moisture content by means of self-sustained smoldering combustion, *Proceedings of the Combustion Institute*, 36 (2017) 4419-4426.
- [18] T.L. Rashwan, J.I. Gerhard, G.P. Grant, Application of self-sustaining smoldering combustion for the destruction of wastewater biosolids, *Waste Management*, (2016).
- [19] S. Whitaker, Simultaneous Heat, Mass, and Momentum Transfer in Porous Media: A Theory of Drying, in: J.P. Hartnett, T.F. Irvine (eds.) *Advances in Heat Transfer*, Vol. 13, Elsevier, 1977, pp. 119-203.
- [20] E. Azhdari, A. Emami, Analytical and numerical study of drying of tomato in non-shrinkage and shrinkage model, *Mathematics and Computers in Simulation*, 166 (2019) 253-265.
- [21] J. Aprajeeta, R. Gopirajah, C. Anandharamakrishnan, Shrinkage and porosity effects on heat and mass transfer during potato drying, *Journal of Food Engineering*, 144 (2015) 119-128.
- [22] D. Dauti, S. Dal Pont, B. Weber, M. Briffaut, N. Toropovs, M. Wyrzykowski, G. Sciumé, Modeling concrete exposed to high temperature: Impact of dehydration and retention curves on moisture migration, *International Journal for Numerical and Analytical Methods in Geomechanics*, 42 (2018) 1516-1530.
- [23] T.L. Rashwan, T. Fournie, J.L. Torero, G.P. Grant, J.I. Gerhard, Scaling up self-sustained smoldering of sewage sludge for waste-to-energy, *Waste Management*, 135 (2021) 298-308.
- [24] T.L. Rashwan, J.L. Torero, J.I. Gerhard, The improved energy efficiency of applied smoldering systems with increasing scale, *International Journal of Heat and Mass Transfer*, 177 (2021) 121548.
- [25] T.L. Rashwan, J.L. Torero, J.I. Gerhard, Heat losses in applied smoldering systems: Sensitivity analysis via analytical modelling, *International Journal of Heat and Mass Transfer*, 172 (2021) 121150.

- [26] T.L. Rashwan, J.L. Torero, J.I. Gerhard, Heat losses in a smouldering system: The key role of non-uniform air flux, *Combustion and Flame*, 227 (2021) 309-321.
- [27] T.K. Sherwood, The Drying of Solids—I, *Industrial & Engineering Chemistry*, 21 (1929) 12-16.
- [28] J.R. Philip, D.A. De Vries, Moisture movement in porous materials under temperature gradients, *Eos, Transactions American Geophysical Union*, 38 (1957) 222-232.
- [29] S. Whitaker, W.T.H. Chou, DRYING GRANULAR POROUS MEDIA - THEORY AND EXPERIMENT, *Drying Technology*, 1 (1983) 3-33.
- [30] V.A.F. Costa, M.L. Mendonça, A.R. Figueiredo, Modeling and simulation of wetted porous thermal barriers operating under high temperature or high heat flux, *International Journal of Heat and Mass Transfer*, 51 (2008) 3342-3354.
- [31] G.N. Ahmed, J.P. Hurst, Modeling Pore Pressure, Moisture, and Temperature in High-Strength Concrete Columns Exposed to Fire, *Fire Technology*, 35 (1999) 232-262.
- [32] S. Messai, M. El Ganaoui, J. Sghaier, L. Chrusciel, G. Slimane, Comparison of 1D and 2D models predicting a packed bed drying, *Int. J. Simul. Multisci. Des. Optim.*, 5 (2014) A14.
- [33] K. Zhang, C. You, Numerical simulation of lignite drying in a packed moving bed dryer, *Fuel Processing Technology*, 110 (2013) 122-132.
- [34] M. Stakić, P. Stefanović, D. Cvetinović, P. Škobalj, Convective drying of particulate solids – Packed vs. fluid bed operation, *International Journal of Heat and Mass Transfer*, 59 (2013) 66-74.
- [35] S.B. Mabrouk, B. Khiari, M. Sassi, Modelling of heat and mass transfer in a tunnel dryer, *Applied Thermal Engineering*, 26 (2006) 2110-2118.
- [36] H. Basirat-Tabrizi, M. Saffar-Avval, M.R. Assarie, Two-dimensional mathematical model of a packed bed dryer and experimentation, *Proceedings of the Institution of Mechanical Engineers, Part A: Journal of Power and Energy*, 216 (2002) 161-168.
- [37] F. Ahmad, M. Talbi, M. Prat, E. Tsotsas, A. Kharaghani, Non-local equilibrium continuum modeling of partially saturated drying porous media: Comparison with pore network simulations, *Chemical Engineering Science*, 228 (2020) 115957.
- [38] C. Borgnakke, R.E. Sonntag, *Fundamentals of Thermodynamics*, 8th Edition, Wiley, 2012.
- [39] M.A.B. Zanoni, J.L. Torero, J.I. Gerhard, Determination of the interfacial heat transfer coefficient between forced air and sand at Reynold's numbers relevant to smouldering combustion, *International Journal of Heat and Mass Transfer*, 114 (2017) 90-104.
- [40] R.B. Bird, W.E. Stewart, E.N. Lightfoot, *Transport Phenomena*, Wiley, 2009.
- [41] L.D. Baver, W.H. Gardner, *Soil Physics*, Wiley, 1972.

- [42] A.K. Datta, Porous media approaches to studying simultaneous heat and mass transfer in food processes. II: Property data and representative results, *Journal of Food Engineering*, 80 (2007) 96-110.
- [43] J. Bear, *Dynamics of Fluids in Porous Media*, Dover, 1988.
- [44] R.E. Sonntag, C. Borgnakke, G.J. Van Wylen, *Fundamentals of Thermodynamics*, Wiley, 2002.
- [45] M. Kaviany, *Principles of Heat Transfer in Porous Media*, Springer, 1995.
- [46] A. Halder, A. Dhall, A.K. Datta, An Improved, Easily Implementable, Porous Media Based Model for Deep-Fat Frying: Part I: Model Development and Input Parameters, *Food and Bioprocess Processing*, 85 (2007) 209-219.
- [47] A.L. Buck, New Equations for Computing Vapor Pressure and Enhancement Factor, *Journal of Applied Meteorology and Climatology*, 20 (1981) 1527-1532.
- [48] M. Bittelli, F. Ventura, G.S. Campbell, R.L. Snyder, F. Gallegati, P.R. Pisa, Coupling of heat, water vapor, and liquid water fluxes to compute evaporation in bare soils, *Journal of Hydrology*, 362 (2008) 191-205.
- [49] A. Mhimid, J.P. Fohr, S. Ben Nasrallah, HEAT AND MASS TRANSFER DURING DRYING OF GRANULAR PRODUCTS BY COMBINED CONVECTION AND CONDUCTION, *Drying Technology*, 17 (1999) 1043-1063.
- [50] M.A.B. Zanoni, J.L. Torero, J.I. Gerhard, The role of local thermal non-equilibrium in modelling smouldering combustion of organic liquids, *Proceedings of the Combustion Institute*, 37 (2019) 3109-3117.
- [51] D.A. Tzempelikos, D. Mitrakos, A.P. Vouros, A.V. Bardakas, A.E. Filios, D.P. Margaritis, Numerical modeling of heat and mass transfer during convective drying of cylindrical quince slices, *Journal of Food Engineering*, 156 (2015) 10-21.
- [52] M.A.B. Zanoni, J. Wang, J.I. Gerhard, Understanding Pressure Changes in Smouldering Thermal Porous Media Reactors, *Chemical Engineering Journal*, (2021) 128642.
- [53] F.P. Incropera, *Fundamentals of heat and mass transfer*, John Wiley, 2007.
- [54] M.A.B. Zanoni, J.L. Torero, J.I. Gerhard, Determining the conditions that lead to self-sustained smouldering combustion by means of numerical modelling, *Proceedings of the Combustion Institute*, 37 (2019) 4043-4051.
- [55] M.A.B. Zanoni, J.L. Torero, J.I. Gerhard, Delineating and explaining the limits of self-sustained smouldering combustion, *Combustion and Flame*, 201 (2019) 78-92.

- [56] J.L. Torero, J.I. Gerhard, M.F. Martins, M.A.B. Zanoni, T.L. Rashwan, J.K. Brown, Processes defining smouldering combustion: Integrated review and synthesis, *Progress in Energy and Combustion Science*, 81 (2020) 100869.
- [57] M.A.B. Zanoni, J.L. Torero, J.I. Gerhard, Experimental and numerical investigation of weak, self-sustained conditions in engineered smouldering combustion, *Combustion and Flame*, 222 (2020) 27-35.
- [58] C. Gorse, D. Johnston, M. Pritchard, *A Dictionary of Construction, Surveying, and Civil Engineering*, OUP Oxford, 2012.
- [59] M.F. Martins, S. Salvador, J.F. Thovert, G. Debenest, Co-current combustion of oil shale - Part 2: Structure of the combustion front, *Fuel*, 89 (2010) 133-143.